



Computational transport, phase change and deposition analysis of inhaled multicomponent droplet–vapor mixtures in an idealized human upper lung model



Yu Feng^a, Clement Kleinstreuer^{a,b,*}, Nicolas Castro^c, Ali Rostami^c

^a Department of Mechanical and Aerospace Engineering, North Carolina State University, Raleigh, NC 27695-7910, USA

^b Joint UNC-NCSU Department of Biomedical Engineering, North Carolina State University, Raleigh, NC 27695-7910, USA

^c Altria Client Services LLC., Research, Development and Engineering, 601 East Jackson Street, Richmond, VA 23219, USA

ARTICLE INFO

Article history:

Received 23 December 2015

Received in revised form

29 February 2016

Accepted 2 March 2016

Available online 14 March 2016

Keywords:

Hygroscopic droplet growth

Multi-component droplet–vapor interaction modeling

Multi-component mixture plus discrete-droplet (MCM-DD) model

Inhaled droplet–reduction (IDR) method

Electronic cigarettes

ABSTRACT

Numerous inhalable aerosols consist of multiple nano-to-microscale solid or liquid particles with dissolved or embedded compounds, as well as associated vapors. In general, of interest are the transport and conversion phenomena leading to local particle/droplet/vapor depositions. Selected examples include inhalation of aerosols from use of inhalers, cigarettes and electronic cigarettes. In this study the focus is on hygroscopic growth of nano-size multi-component droplets and droplet–vapor interactions during transport with subsequent deposition in a human upper lung–airway model. For that purpose a comprehensive and efficient computational fluid–particle dynamics model has been developed. It is capable of simultaneously analyzing multi-component droplet–vapor and airflow interactions with evaporation and condensation effects for different sets of inhalation conditions. Selecting inhaled electronic cigarette (EC) aerosols as an application, the simulation results include detailed transport, deposition and absorption data for different constituents (i.e., water, propylene glycol, glycerol and nicotine) in both vapor and liquid forms for an idealized human upper lung airway geometry, i.e., from mouth to generation 3. Results indicate that liquid–vapor phase change induces hygroscopic growth of droplets, which in turn impacts significantly the deposition concentrations of aerosols via inertial impaction, secondary flows, Brownian motion, and the vapor-specific absorption rates. Parametric sensitivity analyses were performed to evaluate the influence of different inhalation flow waveforms on EC-aerosol transport, interaction, and deposition.

© 2016 Elsevier Ltd. All rights reserved.

1. Introduction

Inhalable liquid aerosols generated from selected sources such as inhalers, drug delivery devices, cigarettes and electronic cigarettes involve complex physical and thermodynamic interactions between, air, vapor, particles and respiratory tract walls. Electronic cigarette (EC) aerosols typically contain interacting droplet–vapor mixtures with nicotine, glycerol,

* Corresponding author at: Department of Mechanical and Aerospace Engineering, North Carolina State University, Raleigh, NC 27695-7910, USA. Tel.: +1 919 515 5216; fax: +1 919 515 7968.

E-mail address: ck@ncsu.edu (C. Kleinstreuer).

$$S_{v-d}^{(E)}$$

$S_{v-d}^{(E)}$	latent heat of evaporation or condensation which is released or absorbed by the droplets per local mesh cell
Sc	Schmidt number $Sc = \nu/D_{a-v}$
SF	scaling factor
Sh	Sherwood number
	$Sh = (1 + Re_d Sc)^{1/3} \max \left[1, Re_d^{0.077} \right]$
t	time
T	temperature
TDF	total deposition fraction
U	continuous phase (air–vapor mixture) velocity
u_d	droplet velocity

 $\|\vec{V}\|$ fluid velocity magnitude

X	mole fraction
Y	mass fraction

Greek symbols

α_m	mass accommodation coefficient $\alpha_m=1$
α_r	thermal accommodation coefficient $\alpha_r=1$
$\beta_{v-l,s}$	vapor-liquid mass change percentage of the sth species
γ_s	activity coefficient of species s
Δt_d	DPM time step
Δt_f	flow time step
λ	mean free path
ν	kinetic molecular viscosity
ρ_{a-v}	air-vapor mixture density
ρ_d	droplet density
ρ_A	surface/area density [kg/m ²]
$\Gamma_{s,w}$	wall absorption coefficient for the sth vapor species
τ	viscous shear stress
σ	surface tension
Φ	dissipation function
μ	dynamic viscosity
\vec{v}	fluid velocity
$\vec{\omega}$	fluid vorticity

Subscripts

<i>A</i>	area
<i>abs</i>	absolute
<i>air</i>	dry air
<i>a-m</i>	air-mucus layer
<i>a-v</i>	air-vapor mixture (continuous phase)
<i>cond</i>	condensation
<i>d</i>	droplet or liquid phase
<i>env</i>	environmental or ambient
<i>eq</i>	equilibrium
<i>H₂O</i>	water
<i>i</i>	tensor index

<i>j</i>	tensor index	<i>vsurf</i>	vapor at the droplet surface
<i>k</i>	droplet index	<i>w</i>	wall
<i>l</i>	liquid form		
<i>v-l</i>	vapor–liquid		
<i>m</i>	mass or mucus layer	<i>Superscripts</i>	
<i>s</i>	component index	<i>dep</i>	deposition
<i>T</i>	thermal	<i>E</i>	energy
<i>tot</i>	total	<i>in</i>	inflow
<i>v</i>	vapor phase or vapor form	<i>ini</i>	initial
<i>v-d</i>	vapor–droplet	<i>out</i>	outflow
<i>vsat</i>	saturated vapor	<i>sus</i>	suspended

propylene glycol (PG) and added flavors. Understanding the vapor particle interactions and dynamics of aerosol transport and deposition is important because these micro-scale phenomena ultimately determine the fate of the inhaled aerosols.

In contrast to experimental and clinical studies, numerical methods, i.e., computational fluid–particle dynamics (CF–PD) simulations, provide a non-invasive, and relatively inexpensive way to predict local deposition and absorption data for different constituents in both vapor and liquid forms. Results from validated computer simulation models can inform and strengthen the scientific understanding of lung deposition patterns expected from various electronic cigarettes.

As recently reviewed by [Tian, Hindle, Lee, and Longest \(2015\)](#), there are different types of numerical models for exposure studies of which semi-empirical and 1-D whole-lung models are most frequently used. In contrast to these two approaches, CF–PD models are based on first principles of physics with a minimum number of empirical correlations. Papers discussing the fate of inhaled EC aerosols include [Manigrasso, Buonanno, Stabile et al. \(2015\)](#) and [Manigrasso, Buonanno, Fuoco et al. \(2015\)](#) who computed the EC-particle deposition fractions in a stochastic lung model using the Multiple-Path Particle Dosimetry approach. However, by neglecting droplet–vapor phase change during transport, they were not able to provide deposition data for the accumulated mass dose of different constituents after EC-aerosol inhalation. Recently, using a CF–PD model, [Schroeter et al. \(2016\)](#) investigated size-change dynamics of single-component droplets with different initial diameters in nasal passages under steady-state inspiratory conditions. The model can simulate vapor transport; however, without the vapor-concentration changes induced by the evaporation/condensation effects. Several papers ([Behar, Hua, & Talbot, 2015](#); [Lee, Gawron, & Goniewicz, 2015](#); [Vansickel, Edmiston, Liang, Duhon, Liu, & Sarkar, 2014](#); among others) investigated puffing behavior and nicotine uptake when using ECs. [Behar et al. \(2015\)](#) investigated the intake of different EC products and claimed that realistic inhalation flow rates range from 12 ml/s to 26 ml/s and the puff duration is from 1.67 s to 3.63 s. [Lee et al. \(2015\)](#) also measured the puff volume and flow rate of different smokers. [Evans and Hoffman \(2014\)](#) reviewed contributions before 2014 on puffing topography when using EC. Generally, cigarette smoker who use E-cigarette take shorter puffs at higher puff rate, while experienced E-cigarette users take longer puffs at lower air volume rate ([Vansickel et al., 2014](#)). Longer puffs for EC consumption were reported when compared to TC consumptions. It has been reported that the intake concentrations of vapor species and droplet number will not be influenced by the inhalation flow rate for EC smoking which is not true for conventional cigarette smoking (see [Talih et al., 2014](#)). However, at high airflow rates, the excessive cooling of the heating element results in reduction of aerosol delivery and particle numbers. Also of great interest is the paper by [Alderman, Song, Moldoveanu, and Cole \(2014\)](#) on measured glycerin, PG and nicotine, generated by several EC products in droplets and vapors.

The major challenges in detailed modeling of the fate of inhaled EC-aerosols arise from the complexities of the very high numbers of polydisperse multi-component droplets, their varying droplet–vapor–air inlet conditions with subsequent size-change dynamics and vapor interactions, large system-scale variations, as well as the non-uniform geometries of any given representative or subject-specific respiratory system. For example, existing CF–PD models neglect the interactions between droplets and vapors during their transport; however, those mechanisms are essential for an improved understanding and a better prediction of local aerosol transport and deposition. We developed a comprehensive Multi-Component Mixture plus Discrete Droplet (MCM–DD) model, which is capable of simultaneously analyzing multi-component droplet–vapor airflow interaction dynamics with evaporation and condensation effects for any set of inhalation conditions. Specifically, the major mechanisms covered by the MCM–DD model are: direct vapor species deposition, vapor species deposition from evaporation, direct liquid species deposition in droplets, and liquid species deposition by condensation. Not being limited to cigarette smoke, the general MCM–DD model is capable of simulating the transport and deposition of other inhalable droplet–vapor aerosol mixtures as well.

The present study provides results on the local deposition of different species in the multicomponent droplet–vapor aerosol mixture when using ECs. Specifically, the significance of droplet–vapor interaction with phase-change, the impact of different puff topographies (i.e., steady-state and transient waveforms with different holding durations), parametric sensitivity analyses on EC aerosol transport and deposition in the idealized human upper lung airway geometry (from mouth to G3) are discussed. The impact of E-liquid composition which affects the liquid vapor partitioning, such as the activity coefficient can also be taken into account. In addition, because of the sheer number of inhaled particles, the inhaled droplet–

reduction (IDR) method is introduced to gain realistic simulation results for liquid–vapor interactions at reasonable computational cost.

2. Theory

To encompass the major mechanisms based on first principles, we developed a comprehensive, accurate and efficient CF–PD solver, which entails the MCM–DD and IDR models. It is capable of simultaneously simulating, for any set of puffing/inhalation conditions, multi-component droplet–vapor airflow dynamics with evaporation and condensation effects during their transport in human respiratory systems. The governing equations are outlined next.

2.1. Continuous phase (air–vapor mixture) transport

Any given air–vapor mixture is described as a single continuous phase, i.e., the conservation laws for mass, momentum and energy describe the air–vapor mixture transport and the advection–diffusion equation describes vapor–species transport. Droplet–vapor interaction, i.e., liquid–vapor mass change due to evaporation or condensation, are implemented by: (i) introducing source terms into the energy equation and vapor–species transport equations (see Eqs. (1)–(4)); and (ii) employing the local vapor–mass fraction in the droplet mass conservation equation (see Eq. (5)). Specifically, the energy equation of the air–vapor mixture reads:

$$\frac{\partial(\rho c_p T)_{a-v}}{\partial t} + \frac{\partial(\rho c_p u_j T)_{a-v}}{\partial x_j} = \frac{\partial}{\partial x_j} \left[\left(k_{a-v} + \frac{\rho_{a-v} c_{a-v,p} \nu_T}{Pr_T} \right) \frac{\partial T_{a-v}}{\partial x_j} \right] + \Phi + \frac{\partial}{\partial x_j} \left[\sum_{s=1}^N h_s \rho_{a-v} \left(\tilde{D}_{a-v} + \frac{\nu_T}{Sc_T} \right) \frac{\partial Y_s}{\partial x_j} \right] + S_{v-d}^{(E)} \quad (1)$$

In Eq. (1), the energy source term $S_{v-d}^{(E)}$ is the latent heat of evaporation or condensation which is released or absorbed by the droplets per local mesh cell:

$$S_{v-d}^{(E)} = \sum_{s=1}^N S_{v-d,s}^{(E)} = \left\{ \sum_{i=1}^{N_{d,cell}} \left[\left(\sum_{s=1}^N L_s \bar{j}_s \right) A_d \right]_i \right\} / V_{cell} \quad (2)$$

where $N_{d,cell}$ is the total droplet number in a specified mesh cell.

The governing equation for advection and diffusion of the sth vapor species are expressed as

$$\frac{\partial(\rho_{a-v} Y_{s,v})}{\partial t} + \frac{\partial(\rho_{a-v} u_j Y_{s,v})}{\partial x_j} = \frac{\partial}{\partial x_j} \left[\rho_{a-v} \left(\tilde{D}_{a-v,s} + \frac{\nu_T}{Sc_T} \right) \frac{\partial Y_{s,v}}{\partial x_j} \right] + S_{v-d,s}^{(Y)} \quad (3)$$

where $Sc_T = 0.9$ is the turbulence Schmidt number, ν_T is the turbulent viscosity, and $\tilde{D}_{a-v,s}$ is the molecular diffusivity of sth vapor species in the air–vapor mixture. The local vaporized/condensed vapor–mass flow rate of the aerosol components are added to its advection–diffusion equation as a source term $S_{v-d,s}^{(Y)}$ ($\text{kg m}^{-3} \text{s}^{-1}$), i.e.,

$$S_{v-d,s}^{(Y)} = \int_{t_{i,start}}^{t_{i,start} + \Delta t_f} \left(\sum_{i=1}^{N_{d,cell}} (\bar{j}_s A_d)_i \right) dt_d / (V_{cell} \Delta t_f) \quad (4)$$

where \bar{j}_s is the average evaporation/condensation mass flux normal to the droplet surface of the sth component (i.e., $\bar{j}_s > 0$ for evaporation and $\bar{j}_s < 0$ for condensation); and A_d is the droplet surface area. Also, dt_d represents the droplet phase time differential and Δt_f is the flow time-step.

2.2. Multicomponent droplet size-change and transport

The Lagrangian approach is chosen to track multi-component droplets, neglecting rotational motion, if any. The governing equations for discrete droplets are the translational equation of droplets as well as the mass and energy conservation laws for droplets.

2.2.1. Translational equation of droplets

Newton's second law of motion states:

$$\frac{d}{dt}(m_d u_{d,i}) = F_i^D + F_i^L + F_i^{BM} + F_i^G \quad (5)$$

where F_i^D , F_i^L , F_i^{BM} , and F_i^G are the drag force, lift force, Brownian motion-induced force, and gravity, respectively.

2.2.2. Mass conservation of droplets

Droplet mass changes due to condensation/evaporation can be described as

$$\frac{dm_d}{dt} = - \sum_{s=1}^N \int_{surf} j_s dA \approx - \sum_{s=1}^N (\bar{j}_s \cdot A_d) \quad (6)$$

where the average mass flux \bar{j}_s is given by Turns (1996):

$$\bar{j}_s = \rho_{a-v} \cdot C_m \cdot Sh \cdot \tilde{D}_{a-v,s} \cdot d_d^{-1} \ln[(1 - Y_{s,v,cell}) / (1 - Y_{s,v,surf})] \quad (7)$$

Here, Sh is the Sherwood number (see the Nomenclature for definition), while $Y_{s,v,surf}$ and $Y_{s,v,cell}$ are the mass fractions of sth vapor phase at the droplet surface and at the center of the cell where the droplet currently resides. The correction factor C_m for submicron droplets, considering non-continuum effects, can be expressed as

$$C_m = \frac{1 + Kn}{1 + \left(\frac{4}{3\alpha_m} + 0.377\right)Kn + \frac{4}{3\alpha_m}Kn^2} \quad (8)$$

where Kn is the Knudsen number, $Kn = 2\lambda_{a-v}/d_d$, in which λ_{a-v} is the mean free path of the air–vapor mixture surrounding the droplet; and α_m is the mass accommodation coefficient, where $\alpha_m = 1$ was used in the present study (Hinds, 1999). The derivation of Eq. (7) is based on the assumption that the distance between the droplet mass center and the mesh cell center is much larger than the droplet radius. Specifically, $Y_{s,v,cell}$ is determined by the advection–diffusion equation (see Eq. (3)), while $Y_{s,v,surf}$ can be calculated by

$$Y_{s,v,surf} = \frac{\rho_{s,v,surf}}{\rho_{a-v}} = \frac{(P_{s,v,surf}/\mathcal{R}_s T_d)}{\rho_{a-v}} = \frac{\gamma_s \cdot K_s \cdot X_{s,d} \cdot P_{s,vsat}(T_d)}{\rho_{a-v}(\mathcal{R}/M_s)T_d} \quad (9)$$

Here, $\rho_{s,v,surf}$ is the equivalent density of vapor species s in the air–vapor mixture at the droplet surface; γ_s is the activity coefficient of species s , which is a correction of the evaporation/condensation characteristics of a certain liquid component due to the molecular bonding changes in the pure droplets and in the multicomponent droplets (Tu & Ray, 2005); $X_{s,d}$ is the mole fraction of the sth component in the droplet; \mathcal{R}_s is the species gas constant; T_d is the droplet temperature; and $P_{s,vsat}$ is the temperature-dependent saturation pressure of the pure sth species. Clearly, parameters γ_s and $X_{s,d}$ serve as corrections to the vapor pressure at the surface of multicomponent droplets (Raoult's law), while K_s is the correction factor for the Kelvin effect (Hinds, 1999):

$$K_s = \exp[4\sigma_s M_s / (\mathcal{R} \rho_s d_d T_d)] \quad (10)$$

where σ_s is the surface tension of component s at the droplet surface.

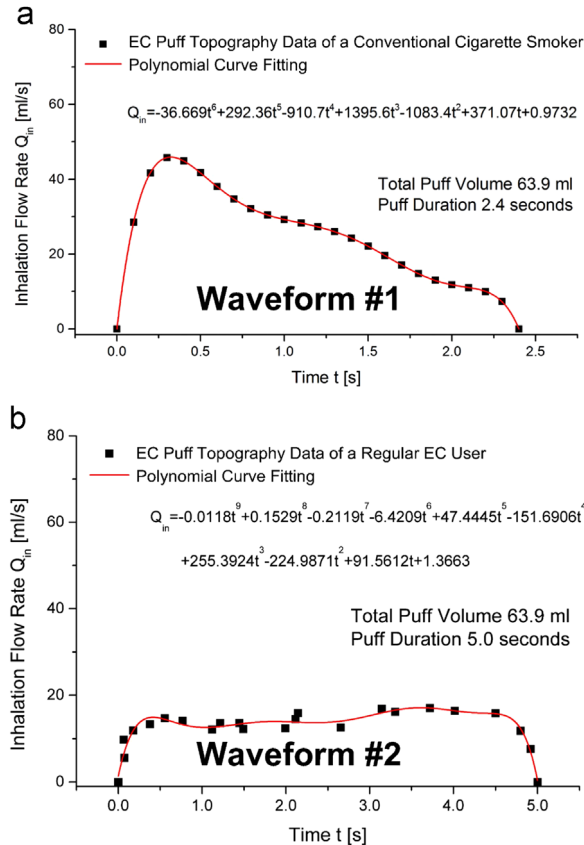


Fig. 1. Realistic EC puff topographies (Vansickel et al., 2014): (a) Waveform #1 typical of a conventional cigarette smoker and (b) Waveform #2 typical of a regular EC user.

2.2.3. Energy conservation of droplets

The droplet heat transfer equation takes on the form:

$$m_d c_{p,d} (dT_d/dt) = C_T (k_{a-v} \cdot Nu/d_d) (T_{a-v,cell} - T_d) A_d - \left(\sum_{s=1}^N L_s \bar{j}_s \right) A_d \quad (11)$$

where L_s is the latent heat of liquid–vapor phase transition of the sth species (L_s is always larger than zero). Also, C_T is the correction factor for submicron droplets:

$$C_T = \frac{1 + Kn}{1 + \left(\frac{4}{3\alpha_T} + 0.377 \right) Kn + \frac{4}{3\alpha_T} Kn^2} \quad (12)$$

where α_T is the thermal accommodation coefficient with the value of $\alpha_T = 1$ (Hinds, 1999).

2.3. Boundary conditions

For realistic numerical simulations of EC-aerosol transport and deposition in human respiratory systems, initial and boundary conditions for different variables were selected in plausible ranges from the open literature.

2.3.1. Mouth-inlet conditions

Considering first steady inlet conditions, an average inlet velocity was determined from a representative inhalation flow rate at mouth-inlet, i.e., $Q_{in} = 27.5$ ml/s (Canada, 2014). The average inlet velocity was 0.5459 m/s, while the inlet aerosol temperature was 360.15 K. That flow rate was also chosen for the mesh-independence test. Then, for parametric sensitivity analyses, different steady-state inhalation flow rates ($Q_{in} = 12$ ml/s, 20 ml/s, and 27.5 ml/s), puffing durations (2 s and 3 s), and holding durations (0 s and 1 s) were selected, representing different EC-puffing/inhalation behaviors (Behar et al., 2015; Lee et al., 2015; among others). For example, Waveform #1 is typical for conventional cigarette smokers switching to ECs, with a puffing duration of 2.4 s and a total volume of 63.9 ml (see Fig. 1(a)). Waveform #2 (see Fig. 1(b)) was based on regular EC-users, where the puffing duration is 5.0 s but the total volume remains at 63.9 ml.

To simulate continuous inhalation of EC droplets, multiple droplet injections were generated based on random-parabolic droplet distributions at the mouth inlet, using an in-house MatLab[®] code (Feng et al., 2015). The droplet initial diameter was uniformly 400 nm, which represents the MMD of a realistic EC droplet size distribution (Alderman et al., 2014). Liquid–vapor partitions and other initial inputs (see Table 1) were in reasonable ranges, considering the most recent EC aerosol measurements (Alderman et al., 2014; among others).

2.3.2. Boundary conditions for multicomponent droplet and vapor depositions

To evaluate potential uptake of certain components in EC aerosols, accurate calculations of the locally deposited/absorbed amounts are of great importance; hence, realistic wall boundary conditions for droplet and vapor deposition/absorption are necessary.

2.3.2.1. Droplet deposition boundary condition. Droplet deposition occurs when its mass center comes within the droplet radius from the wall. The species mass deposited in the droplet with index k is calculated as

$$\left[m_{s,l}^{(dep)} \right]_k = \left[m_d Y_{s,d} \right]_k \quad (13)$$

where s is the species index, and $Y_{s,d}$ is the mass fraction of the sth species in the deposited droplet.

2.3.2.2. Vapor absorption boundary condition. Vapor absorption at human lung-airway surfaces is a function of tissue solubility, which is related to the air–lung partitioning ratio. In the present study, quasi-steady equilibrium at the air–mucus

Table 1

Initial and boundary conditions for simulating injection of EC droplet–vapor mixture.

Droplet initial diameter	400 nm			
Initial droplet density	1106.70 kg/m ³			
Inlet air flow rate	From 12 ml/s to 27.5 ml/s			
Total e-cigarette aerosol mass flow rate	4.17 mg/s for 27.5 ml/s			
Inlet temperature	360.15 K			
Inlet relative humidity	50.00%			
Vapor–liquid mass fraction partitions (wt/wt)	Water	Glycerol	PG	Nicotine
	N/A	0.1293%	18.20%	5.09%
Initial air–vapor mixture density	1.2842 kg/m ³			
Initial vapor species mass fraction	Water	Glycerol	PG	Nicotine
	1.98%	0.0048%	0.75%	0.013%
Initial droplet component mass fraction	Water	Glycerol	PG	Nicotine
	15%	38.96%	43.34%	2.7%

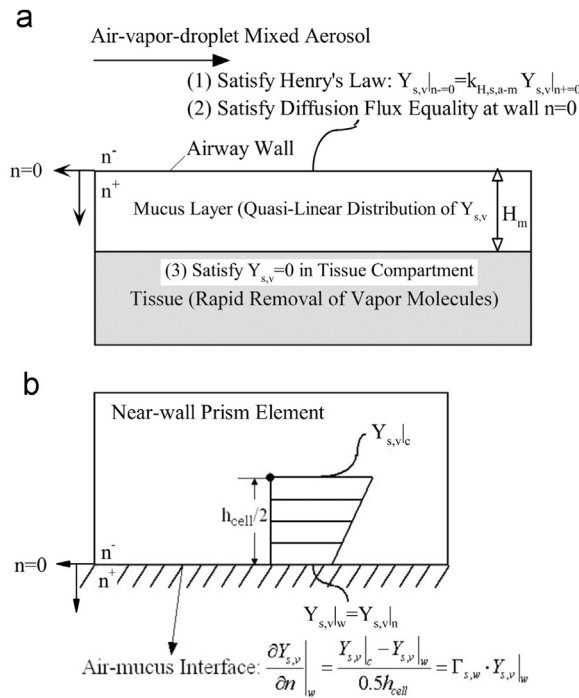


Fig. 2. Mixed vapor absorption boundary condition at air-mucus layer: (a) sketch at the airway wall and (b) numerical treatment.

Table 2

Physical properties of vapor species (at 25 °C and 1 atm).

	$\tilde{D}_{a-v,s}$ [cm ² /s]	$\tilde{D}_{m,s}$ [cm ² /s]	$k_{H,s,a-m}$	$\Gamma_{s,w}$ [cm ⁻¹]
Glycerol	0.0877	9.30e-6 ^a	3.93e-9 ^b	2.70e+7
PG	0.1060	1.23e-5 ^c	4.90e-7 ^d	2.39e+5
Nicotine	0.0650 ^e	8.60e-6 ^f (in epithelium)	3.31e-7 ^g	4.00e+5

Notes:

(1) Values of $\tilde{D}_{m,s}$ are approximated by the values in water unless otherwise noted.

(2) The dimensionless gas-liquid Henry's law constants $k_{H,s,a-m}$ are assumed for air-water interface unless otherwise noted. Same assumptions and reasons have been discussed in Keyhani, Scherer, & Mozell (1997). Conversions between different definitions of Henry's law constant provided by <http://www.mpch-mainz.mpg.de/~sander/res/henry.html>.

Data Sources:

^a Hayduk and Laudie (1974).

^b <http://www.inchem.org/documents/sids/sids/56815.pdf>.

^c <http://www.gsi-net.com/en/publications/gsi-chemical-database/single/469.html>.

^d <http://www.atsdr.cdc.gov/toxprofiles/tp189-c3.pdf>.

^e Eatough et al. (1989).

^f Gowadia and Dunn-Rankin (2010).

^g http://tools.niehs.nih.gov/cebs3/ntpviews/index.cfm?action=testarticle.properties&cas_number=54-11-5.

interface (see Fig. 2(a)) and zero concentration below the lipid layer due to the rapid removal of vapor molecules by the tissue were assumed. Specifically, “quasi-steady equilibrium” means that the species concentrations at both sides of the interface always satisfy Henry's law. Thus, the vapor absorption boundary conditions at lung-airway walls ($n=0$) for glycerol, PG and nicotine are:

$$\frac{\partial Y_{s,v}}{\partial n} \bigg|_{n=0} + \Gamma_{s,w} \cdot Y_{s,v}|_{n=0} = 0 \quad (Y_{s,v}|_{n=0} \geq 0) \quad (14)$$

Here, $\Gamma_{s,w}$ is called the wall absorption coefficient for the s th vapor species, which is:

$$\Gamma_{s,w} = \frac{\tilde{D}_{m,s}}{\tilde{D}_{a-v,s} k_{H,s,a-m} H_m} \quad (15)$$

where $\tilde{D}_{a-v,s}$ and $\tilde{D}_{m,s}$ are the vapor diffusivity in the air and the mucus phase, respectively; H_m is the thickness of the mucus layer which is assumed to be 10 μm (Zhang, Kleinstreuer, & Feng, 2012); and $k_{H,s,a-m}$ is the dimensionless gas-liquid

equilibrium partition coefficient (i.e., dimensionless Henry's law constant) for a given vapor species (Pankow, 2001). Specifically, being a third-type boundary condition, Eq. (14) is more realistic than a first- or second-type because it represents the finite absorption rate of vapor species (Keyhani et al., 1997). In contrast, the widely used zero vapor-concentration, i.e., the first-type boundary condition, indicates an infinite absorption rate. Actually, the mucus-layer thickness for healthy human H_m increases from the distal to the proximal lung airways by 50 μm (Fahy & Dickey, 2010), where the average mucus-layer thickness is 15 μm in the mouth-throat region, 11 μm in G1–G3, and 6 μm in G4–G9 (ICRP, 1994; Luchtel, 1978). This justifies an average value of $H_m = 10 \mu\text{m}$ (Table 2).

The calculation procedure for the wall absorption rates of vapor species is based on the numerical treatment documented in Shi, Kleinstreuer, Zhang, and Kim (2004). Assuming that the mass fraction distribution is a linear function of the distance from the near-wall center to the wall (Fig. 2(b)), the wall mass fractions are calculated and updated at each time step according to the mixed boundary condition:

$$\left. \frac{\partial Y_{s,v}}{\partial n} \right|_w = \frac{Y_{s,v}|_c - Y_{s,v}|_w}{0.5h_{\text{cell}}} = \Gamma_{s,w} \cdot Y_{s,v}|_w \quad (16)$$

where $Y_{s,v}|_c$ is the mass fraction at the near-wall mesh cell center, and h_{cell} is the height of the near-wall prism mesh cell. Therefore, $Y_{s,v}|_w$ can be calculated as

$$Y_{s,v}|_w = (1 + 0.5h_{\text{cell}}\Gamma_{s,w})^{-1} Y_{s,v}|_c \quad (17)$$

$Y_{s,v}|_w$ in Eq. (16) is identical to $Y_{s,v}|_{n=0}$ in Eq. (14). After the droplet touches the wall, it is assumed that all the components are rapidly absorbed and will not be able to re-evaporate into the lung airways which behave only as sinks. Thus, the local vapor-species absorption flux by diffusion, without turbulence effects, near the lung airway walls (in $[\text{kg}/(\text{m}^2 \text{ s})]$) reads:

$$j_{s,v}^{(\text{dep})}|_w = -\rho_{a-v}\tilde{D}_{a-v,s}\left.\frac{\partial Y_{s,v}}{\partial n}\right|_w = \rho_{a-v}\tilde{D}_{a-v,s}\Gamma_{s,w} \cdot Y_{s,v}|_w \quad (18\text{a and } 18\text{b})$$

Accordingly, the total mass deposition of one species (e.g., glycerol, PG, or nicotine) can be expressed as the summation of the mass deposition of the species in droplet and vapor forms. Clearly, even under steady inhalation conditions, the total mass deposition is a function of both space and time. The total deposited mass of the sth EC-aerosol species is then:

$$m_s^{(\text{dep})}(t) = m_{s,l}^{(\text{dep})}(t) + m_{s,v}^{(\text{dep})}(t) \quad (19)$$

where $m_{s,l}^{(\text{dep})}(t)$ and $m_{s,v}^{(\text{dep})}(t)$ is the accumulated deposited mass [kg] of the sth species in liquid and vapor forms, respectively, where $m_{s,l}^{(\text{dep})}(t)$ and $m_{s,v}^{(\text{dep})}(t)$ are evaluated using the following equations:

$$m_{s,v}^{(\text{dep})}(t) = \iint j_{s,v}^{(\text{dep})}|_w dt dA \quad (20)$$

and

$$m_{s,l}^{(\text{dep})}(t) = \sum_{k=1}^{N_{\text{dep}}(t)} [m_{s,l}^{(\text{dep})}]_k \quad (21)$$

Here, $j_{s,v}^{(\text{dep})}|_w$ is obtained with Eqs. (18a) and (18b) and $[m_{s,l}^{(\text{dep})}]_k$ by Eq. (13).

2.3.3. Other wall boundary conditions

A constant wall temperature of 37 °C (i.e., 310.15 K) and constant relative humidity (RH) of 99.5% were assumed at the walls of the human respiratory system and uniform (zero) pressure was applied at the eight outlets (see Feng, Kleinstreuer, & Rostami, 2015).

2.4. Deposition calculations of components in EC aerosols

Droplet-vapor mixture deposition in human respiratory systems are traditionally quantified in terms of the deposition efficiency (DE), the deposition fraction (DF), or the deposition enhancement factor (DEF) (see Zhang, Kleinstreuer, & Hyun, 2012; Zhang, Kleinstreuer, & Feng, 2012). However, those variables are not sufficient to provide complete physical insight for aerosol deposition in dual (i.e., liquid and vapor) phases as a result of evaporation and condensation. Thus, to provide more relevant deposition data for different species in the inhaled aerosol mixture, definitions of modified deposition fractions are introduced. Specifically, to measure the deposition fractions of each species in liquid or vapor form, the *deposition fraction based on total species inflow mass* are now defined as

$$DF_{s,v+l}(t) = \frac{m_{s,l}^{(\text{dep})}(t)}{m_{s,l}^{(\text{in})}(t) + m_{s,v}^{(\text{in})}(t)} \quad (22)$$

and

$$DF_{s,v+1}(t) = \frac{m_{s,v}^{(dep)}(t)}{m_{s,l}^{(in)}(t) + m_{s,v}^{(in)}(t)} \quad (23)$$

where $DF_{s,l+1}$ and $DF_{s,v+1}$ are the deposition fractions of sth species in liquid and vapor forms, respectively; where $m_{s,l}^{(in)}(t)$ and $m_{s,v}^{(in)}(t)$ are the total inflow mass of the sth species in liquid and vapor forms. Hence, the deposition fraction of the sth species $DF_s(t)$ is the summation of $DF_{s,l+1}$ and $DF_{s,v+1}$. However, because of the strong variations in liquid–vapor partitions and mass exchanges, it is also necessary to introduce a vapor deposition fraction based on vapor species inflow mass $DF_{s,v}(t)$ as well as a liquid deposition fraction based on liquid species inflow mass $DF_{s,l}(t)$:

$$DF_{s,v}(t) = \frac{m_{s,v}^{(dep)}(t)}{m_{s,v}^{(in)}(t)} \quad (24)$$

and

$$DF_{s,l}(t) = \frac{m_{s,l}^{(dep)}(t)}{m_{s,l}^{(in)}(t)} \quad (25)$$

2.5. Inhaled droplet-reduction (IDR) method

For realistic simulations of EC droplet–vapor interactions the very high number density of injected droplets (i.e., $5.5e+10/\text{cm}^3$) has to be considered, which implies considerable computational cost when using the Lagrange tracking scheme. In order to reduce the computational time, a minimal, scaled-down droplet-number flow rate $Q_{N,inj}$ [#/ (ml s)] has to be considered, representing the impact of the real droplet-number flow rate $Q_{N,real}$ [#/ (ml s)]. This task has been accomplished with the “inhaled droplet-reduction” (IDR) method which must satisfy two requirements:

- The assumed droplet-number flow rate, $Q_{N,inj}$, must be sufficiently high to guarantee particle deposition patterns basically independent of the actual droplet-injection number, $Q_{N,real}$.
- Nevertheless, when using a lower number of inhaled droplets to represent the actual number of droplets generated from the EC, the droplet–vapor interaction rate (i.e., liquid–vapor mass transfer rate) for a single droplet must be modified by a scaling factor to maintain the accuracy of interaction mechanisms between the two phases.
- Expanding from a single droplet to $Q_{N,real}/Q_{N,inj}$ droplets, the original droplet–vapor source term has to be amplified by the $Q_{N,real}/Q_{N,inj}$ ratio.

Indeed, it has been observed from our EC droplet–vapor aerosol transport/deposition simulations that: (a) the total deposition efficiency of the key constituent, i.e., nicotine, converges as the injected droplet number increases; and (b) the single droplet–vapor interaction intensity varies with the increase in droplet number. Based on these facts, the goal is to reduce the computational cost induced by the realistic high droplet-injection number flow rate by correcting droplet–vapor interaction intensities with a scaling factor (SF) which is the kernel of the IDR method. For a single droplet, the liquid–vapor

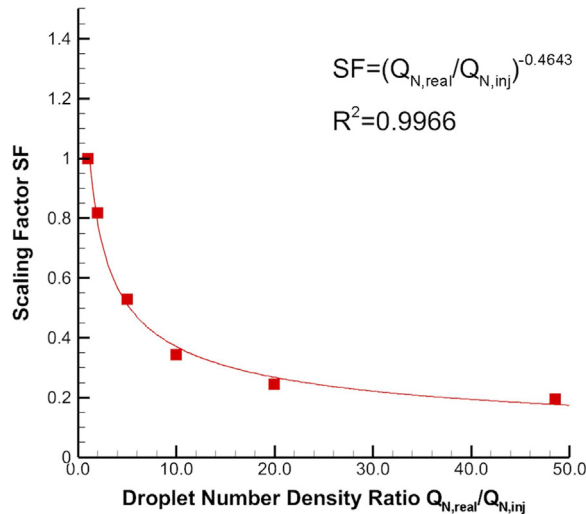


Fig. 3. The relationship between scaling factor SF (i.e., non-dimensionalized single-droplet liquid–vapor interaction intensity) and ratio of droplet number density.

Table 3
Scaling factor (SF) values for different inhalation flow rates.

Q_{in} [ml/s]	Total puff volume [ml]	$Q_{N,real}/Q_{N,inj}$	SF
12 ml/s (for 2 s)	24	0.6634e+7	6.8022e−4
20 ml/s (for 2 s)	40	1.1057e+7	5.3659e−4
27.5 ml/s (for 2 s)	55	1.5203e+7	4.6284e−4
18.3 ml/s (for 3 s)	55	1.0117e+7	5.5918e−4
Transient waveform #1 26.6 ml/s (for 2.4 s)	63.9	1.4705e+7	4.7005e−4
Transient waveform #2 12.78 ml/s (for 5.0 s)	63.9	0.7065e+7	6.6063e−4

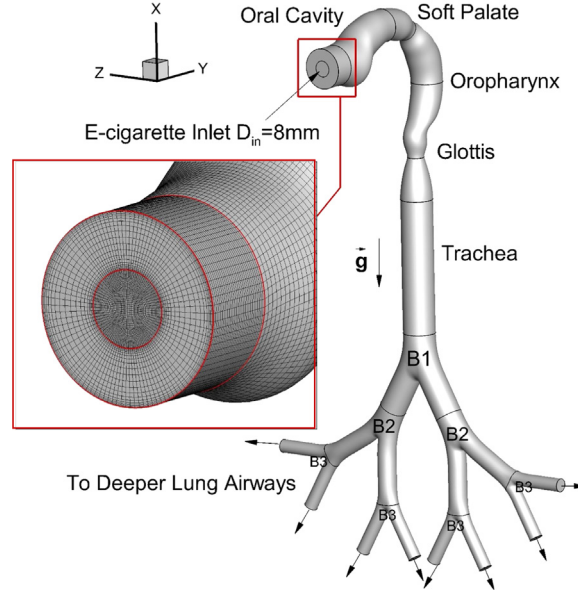


Fig. 4. Configuration and structured hexahedral mesh of idealized human upper respiratory system.

interaction intensity at time t is defined as the mass change percentage due to the condensation or evaporation, where the scaling factor (SF) is the non-dimensionalized single-droplet liquid–vapor interaction intensity adjustment, with the condition that $SF=1$ when $Q_{N,real}=Q_{N,inj}$. Based on computational experiments, an SF-correlation has been determined for a manageable number–density of injected nano-droplets, i.e., presently $Q_{N,inj}=207$ [#/ (ml s)]. This allows to simulate efficiently the droplet–vapor interaction intensity (i.e., correct size-change dynamics) for the actual droplet–number flow rate, $Q_{N,real}$. In summary, the transport and deposition of $Q_{N,inj}=207$ [#/ (ml s)] with corrected size-change dynamics due to evaporation/condensation can statistically represent the real droplet–number flow rate $Q_{N,real}$.

The SF-correlation, being a function of $Q_{N,real}/Q_{N,inj}$, has been obtained from the single droplet–vapor interaction intensity data shown in Fig. 3:

$$SF = (Q_{N,real}/Q_{N,inj})^{-0.4643} \quad (26)$$

It is assumed that (1) this relationship is equally valid for other constituents in the aerosol and (2) it is geometry independent. The SF-values for different inhalation conditions used in the present study are listed in Table 3. Assuming that the SF-correlation will not be influenced by variations of droplet composition and size, the average evaporation/condensation mass flux \bar{j}_s (see Eq. (7)) can be modified as

$$\bar{j}_s = SF \cdot \rho_{a-v} \cdot C_m \cdot Sh \cdot \tilde{D}_{a-v,s} \cdot d_d^{-1} \ln[(1 - Y_{s,v,cell}) / (1 - Y_{s,v,surf})] \quad (27)$$

Expanding from a single droplet to $Q_{N,real}/Q_{N,inj}$ droplets, the original droplet–vapor source term (see Eq. (4)) needs to be amplified by $Q_{N,real}/Q_{N,inj}$ as follows:

$$S_{v-d,s}^{(Y)} = \frac{Q_{N,real}}{Q_{N,inj}} \int_{t_{i,start}}^{t_{i,start} + \Delta t_f} \left(\sum_{i=1}^{N_{d,cell}} (\bar{j}_s A_d)_i \right) dt_d / (V_{cell} \Delta t_f) \quad (28)$$

Accordingly, the numerical calculations of the species deposition in liquid and vapor forms are updated as well:

$$DF_{s,v+l}(t) = \frac{(Q_{N,real}/Q_{N,inj})m_{s,l}^{(dep)}(t)}{(Q_{N,real}/Q_{N,inj})m_{s,l}^{(in)}(t) + m_{s,v}^{(in)}(t)} \quad (29)$$

and

$$DF_{s,v+l}(t) = \frac{m_{s,v}^{(dep)}(t)}{(Q_{N,real}/Q_{N,inj})m_{s,l}^{(in)}(t) + m_{s,v}^{(in)}(t)} \quad (30)$$

In summary, the underlying assumptions for calculating the present SF-correlation are as follows:

- (1) The SF is an averaged function to correct the droplet–vapor interaction difference between actual droplet–injection numbers and assumed injection number.
- (2) The correlation is based on numerical experiments considering transport and conversion for $t=2$ s in a single-airway bifurcation.
- (3) The SF depends only on the droplet–number density ratio between the realistic and the selected case, presently a sufficient injection droplet–number flow rate of $Q_{N,inj}=207$ [#/(ml s)].

3. Numerical simulations

3.1. Geometry and mesh

Based on the dimensions provided by Cheng, Zhou, and Chen (1999), a somewhat idealized but representative mouth-to-trachea and a triple bifurcation unit (TBU) were selected for the present study (see Fig. 4). Thus this configuration covers the oral cavity to G3 with an 8 mm mouth-inlet for the electronic cigarette (EC), where the center coordinate of the EC-inlet is (0, 0, 0). The inhaled airflow is parallel to the positive y -direction and gravity is along the negative x -direction. The bronchial tree lies in the xz -plane.

For the numerical simulation a structured, multi-block, body-fitted hexahedral mesh was developed. The final mesh contained 2,374,679 cells and 2,319,768 nodes. The near-wall cells were refined in element density to resolve any geometric as well as turbulent flow features. The relatively high local mesh resolution is also necessary to accurately calculate values of near-wall derivatives, such as the deposition fluxes. Also, the cells at the boundary of the 8 mm EC mouthpiece (i.e., mouth inlet) are refined (see Fig. 4).

3.2. Mesh independence test

Mesh independence tests were performed using steady flow simulations of air with a mouth inlet temperature of 360.15 K and inlet flow rate of $Q_{in}=27.5$ ml/s. The wall boundary conditions are set to be no-slip with a constant body temperature of 310.15 K, while the outlets were set to be at uniform pressure.

The mesh topologies were determined by refining the meshes until grid independence of the flow field solutions was achieved. For example, three meshes were generated with different mesh densities which are shown in Table 4. Specifically, Mesh 2 was refined by factor 2.0 compared to Mesh 1, and Mesh 3 was also refined by factor 2.0. Mesh independence was investigated by comparing non-dimensionalized velocity profiles at a few selected locations (i.e., cross sections A–A', B–B', and C–C') in the flow domain (see Fig. 5(a)). The non-dimensionalized velocity V^* is defined as

$$V^* = \|\vec{V}\|/\bar{V}_{in} \quad (31)$$

where $\|\vec{V}\|$ is the local velocity magnitude and $\bar{V}_{in}=0.5459$ m/s is the average inlet velocity related to $Q_{in}=27.5$ ml/s.

Considering the velocity profiles at B–B' (i.e., glottis) as an example (see Fig. 5(b)), differences generated with each mesh are visible. While Mesh 1 is too coarse, the variations of simulated velocity profiles were within 1.0% between Mesh 2 and the very fine Mesh 3. So, Mesh 2 was employed as the best mesh when considering both accuracy and computational cost.

Table 4
Best mesh testing for the idealized human upper respiratory system.

Mesh no.	Total number of elements	Total number of nodes	Refinement factor at x, y, or z directions
1	352,901	337,744	N/A
2 (final)	2,374,679	2,319,768	2.0
3	19,755,522	19,528,440	2.0

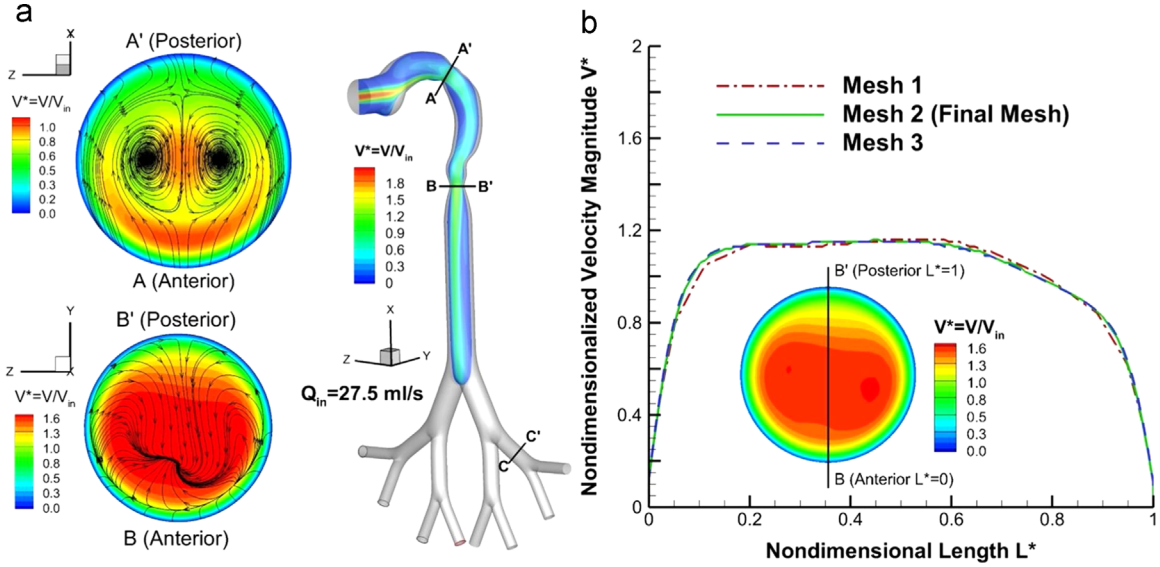


Fig. 5. Mesh-independence test for the idealized human respiratory system: (a) streamlines and velocity contours at cross-sections and the sagittal plane and (b) velocity profiles at the cross-section B–B' computed with different meshes.

3.3. Numerical setup

The computational results of the governing equations with appropriate boundary conditions were achieved with a user-enhanced, commercial finite-volume based program, i.e., ANSYS Fluent 15.0 (ANSYS Inc., Canonsburg, PA). The shear stress transport (SST) transition model was selected to solve for the laminar-to-turbulence airflow fields (Zhang & Kleinstreuer, 2011; Zhang, Kleinstreuer, & Hyun, 2012; Zhang, Kleinstreuer, & Feng, 2012; among others). In the CM-P Lab of the MAE Department at NCSU, numerical simulations were performed on a local Dell Precision T7910 workstation (Intel® Xeon® Processor E5-2670 v3 with 2 processors, 12 cores and 64 GB RAM), of which 6–8 cores were used for the transient inhalation case with the IDR method. Typical run times were approximately 72–96 h. The supplementary user-defined functions (UDFs) are able to perform the following tasks:

- Initializing and defining of input variables
- Customizing the time step for the discrete phase model (DPM)
- Defining realistic transient inhalation waveforms
- Recovering Brownian-motion induced droplet velocities
- Calculating multicomponent droplet-size change dynamics considering interactions with ambient vapor species
- Defining diffusivities, droplet–vapor interaction source terms, and boundary conditions of the transport equations for vapor species
- Calculating and recording local deposition and absorption of EC components in both droplet and vapor forms.

In addition to the UDFs, a MatLab® program for random droplet distributions was implemented at different flow time steps, starting from the mouth inlet.

The flow time step has to be relatively small, i.e., 0.0001 s, which is restricted by the convergence requirements induced by the droplet–vapor interaction calculations. The DPM time step was determined, following Gupta and Peters (1985), i.e.,

$$\Delta t_d \approx \frac{3\pi\mu_{a-v}d_{d,ini}}{C_c m_{d,ini}} \quad (32)$$

The rationale for Eq. (32) is as follows:

- The DPM time-step should be much larger than the time interval of two successive collisions between droplets and surrounding air molecules; because, the white noise process simulated via the Brownian-motion force is a result of a sufficient number of collisions, i.e., the DPM time step should be much larger than τ_B .
- The DPM time-step should be approximately equal to or slightly larger than the value indicated by Eq. (32), which is the momentum relaxation time. Actually, the white noise process requires that two successive Brownian-force magnitudes, obtained via a Gaussian random number generator, should be independent of each other. To guarantee that, the DPM time step must be equal to or slightly larger than Eq. (32), so that the energy and momentum the droplets obtained during Δt due to Brownian motion can be damped by the dissipation force.

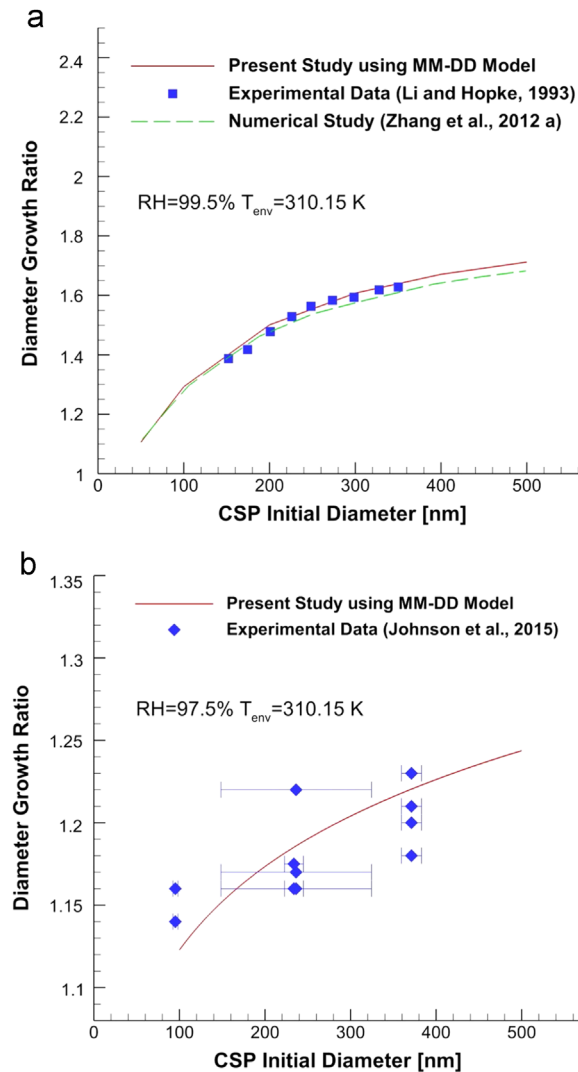


Fig. 6. Model validations for droplet-size change in comparison to experimental data sets: (a) comparison with Li and Hopke (1993) and (b) comparison with Johnson et al. (2015).

(c) The DPM time-step should be much less than the large-scale droplet-residence time, because the frequency of Brownian-motion induced fluctuations is much higher so that the number of fluctuations numerically generated during the transport of the droplets should be sufficiently high.

4. Model validations

Basic model validations are discussed in previous papers (i.e., Feng et al., 2015; Zhang, Kleinstreuer, & Feng, 2012; Zhang, Kleinstreuer, & Hyun, 2012) and in the next sections. Specifically, to validate the new MCM-DD model, the following should be considered:

- droplet-size change dynamics due to evaporation/condensation as part of droplet–vapor interactions (i.e., phase change);
- discrete phase transport and deposition; and
- vapor species transport and deposition.

4.1. Droplet-size dynamics

As previously reported by Feng et al. (2015), Fig. 6(a) shows the comparison of the diameter–growth ratios for conventional cigarette smoke particles (CSP) between the present numerical study and experimental measurements by Li and

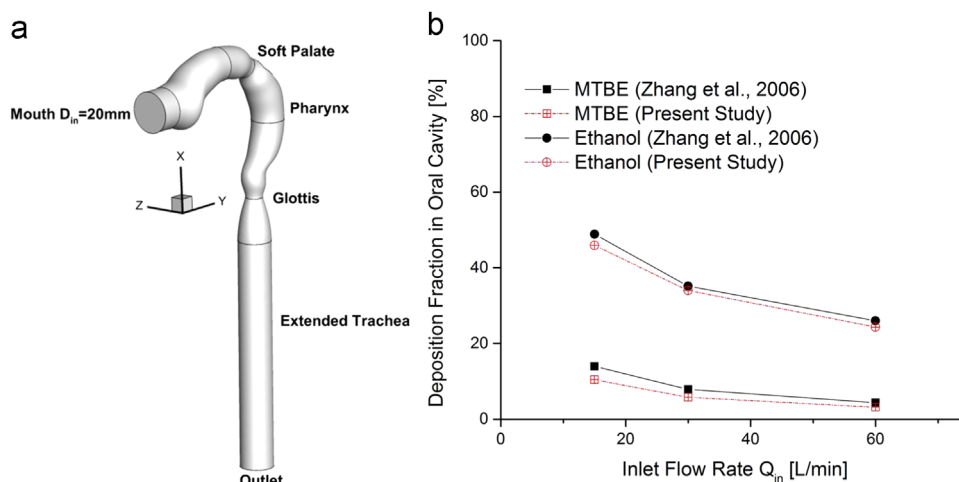


Fig. 7. Model validations for inhaled vapor uptake: (a) Idealized oral cavity geometry with 20 mm circular mouth inlet; (b) Comparison of regional deposition fractions of MTBE and ethanol vapors with inlet flow rates $Q_{in} = 15, 30$, and 60 L/min of 303.15 K .

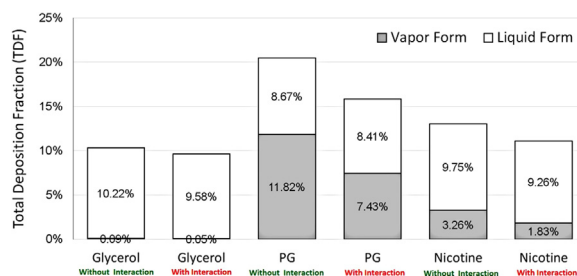


Fig. 8. Total deposition fractions (TDFs) of different EC-aerosol components with or without liquid–vapor interactions in the idealized human upper airway model ($Q_{in} = 27.5\text{ ml/s}$ at $t = 2\text{ s}$).

Hopke (1993) at $RH = 99.5\%$. An additional comparison is shown in Fig. 6(b) between our numerical study and the experimental data of Johnson, Olfert, Yurteri, Cabot, and McAughey (2015) for CSPs with initial diameters ranging from 100 nm to 500 nm at $RH = 97.5\%$. As expected, elevated ambient RH -values lead to higher growth ratios for the CSPs with the same initial diameter. Furthermore, with the increase in initial diameter, the growth ratio increases for CSPs under the same ambient RH . These observations were also confirmed by Johnson et al. (2015).

4.2. Discrete phase transport and deposition

Validations of the discrete phase transport and deposition model (i.e., particle deposition fractions), based on the Euler–Lagrange method, are documented in our previous publications (Zhang et al., 2004, 2005; Zhang, Kleinstreuer, & Hyun, 2012).

4.3. Vapor species transport and deposition model

For the validation of the multicomponent vapor species transport and deposition model (see Fig. 7(a)), methyl tertiary-butyl ether (MTBE) and ethanol transport and deposition were compared to the benchmark numerical results of Zhang, Kleinstreuer, and Kim (2006). The oral cavity had a 20-mm mouth opening with the extended trachea approximately 14 cm from the outlet to the glottis. The final hybrid tetrahedral/pentahedral mesh was generated with six prism layers near the wall surface. The total number of elements was 999,760. The mouth inlet flow rates, Q_{in} , varied from 15 L/min to 60 L/min . The non-dimensionalized vapor mass fractions at the mouth inlet are 1.0 for both MTBE and Ethanol. The details of wall absorption rate boundary condition are discussed in Section 2.3.2. The SST transition model was selected for simulating the laminar-to-turbulence airflow, where residual constraints were set at $1e-4$ for continuity, momentum, energy, and turbulent flow equations, while $1.0e-6$ was set for the vapor–mass transport equations. Figure 7(b) shows the comparison of deposition fractions of MTBE and ethanol vapors in the oral cavity for different inlet flow rates ($Q_{in} = 15, 30$, and 60 L/min). The small differences between the current simulation and the result of Zhang et al. (2006) are due to the following reasons:

- Different models for laminar-to-turbulence transition flow were employed.

- A different length for the trachea extension was employed.

In summary, these validations instill confidence that the MCM-DD model is accurate enough to numerically simulate vapor transport and absorption in human lung airways.

5. Results and discussion

5.1. Prediction of liquid–vapor interaction on compound deposition

The significance and hence necessity to include liquid–vapor interaction mechanisms for the prediction of total deposition fractions (TDFs) was investigated. Specifically, two transient cases in the idealized mouth-to-G3 geometry (see Fig. 4) were simulated with and without liquid–vapor interactions, i.e., phase change due to evaporation or condensation effects. Figure 8 depicts (see Table 1) significant TDF differences for PG, glycerol and nicotine between the two cases. Specifically, approximately 7% of glycerol, 29% of PG, and 17% of nicotine deposit less when considering liquid–vapor interactions. In reality all three vapor species condensate during transport, i.e., more of the compounds will be transferred to liquid form and hence moving with the droplets. That leads to lower TDFs in vapor form (see Eq. (23)) because of the lower local vapor concentrations. Additionally, with liquid–vapor interaction, the TDFs in liquid form (see Eq. (22)) are slightly lower due to the combined influence from the increased inertia of the growing droplets and the higher species mass in a single droplet. The comparison in Fig. 8 also indicates that with the increase in species volatility and initial deviation from the equilibrium partition between liquid and vapor form, including the liquid–vapor interaction mechanism becomes very important for accurate TDF predictions.

5.2. EC-aerosol transport and deposition under transient puffing/inhalation conditions

The puffing/inhalation waveform #1 (Fig. 1(a)) is based on measurements of EC inhalation behavior (Behar et al., 2015; Farsalinos et al., 2014; Lee et al., 2015). As discussed, we selected waveform #1 with puff duration 2.4 s and puff volume 63.9 ml, as a representative inhalation scenario (see initial setup shown in Table 1). The regional and total deposition data of PG, glycerol, and nicotine after $t=2.4$ s are listed in Table 5. At the end of the single EC puff ($t=2.4$ s), 10.57% of glycerol, 16.53% PG and 11.95% of nicotine deposited in the upper RT-region from mouth to G3.

5.2.1. Transient airflow structures and vortices visualization during a single EC puff cycle

As the transient airflow structures determine EC droplet–vapor transport and deposition, a detailed analysis of the local airflow patterns is very important. Figures 9 and 10 depict an inlet jet, stagnation point flow, recirculating flow, and secondary flows. The relationship between the airflow field and the one-way coupled transport and deposition patterns of EC aerosols are discussed next.

5.2.1.1. Transient airflow structures. Figure 9(a)–(g) show the airflow field evolution at the sagittal plane ($Z=0$) for the transient puff waveform #1, colored by the velocity magnitude $||\vec{V}||$. At $t=0.1$ s (see Fig. 9(a)), the inlet flow rate starts to increase and a jet stream begins to form. While the developing jet does not impact the lower palate, there are high velocity regions in contracting cross sections such as the connection between oral cavity and pharynx as well as the glottis. At $t=0.2$ s (see Fig. 9(b)), with the increase in air-drawing intensity, the inlet jet is well formed, impacting the lower palate. The jet core deviates due to impaction and extends to the back of the pharynx. The pressure difference induced by the velocity difference inside and outside the jet core causes the formation of recirculation regions, as seen near the upper palate, lower palate and the inner region of the pharynx (see red-dash circles in Fig. 9(b) and (c)). Clearly, droplets suspended in those recirculation regions have a longer residence time and will less likely deposit. At $t=0.4$ s, the air-drawing intensity has reached its maximum (actually 47 ml/s at $t=0.3$ s) and the jet-core extends into the trachea and bends towards the front

Table 5

Regional deposition fractions (RDFs) of glycerol, PG, and nicotine after $t=2.4$ s for EC waveform #1 (see Fig. 1 for details).

Accumulated inflow mass at $t=2.4$ s (mg)	Glycerol 2.5041		PG 3.8173		Nicotine 0.2116	
	Vapor	Liquid	Vapor	Liquid	Vapor	Liquid
RDFs (%)						
Oral cavity	0.0391	5.2934	5.3577	4.6288	1.3482	5.0951
Oropharynx	0.0070	2.5045	1.0879	2.2151	0.3057	2.4266
Trachea	0.0010	0.4526	0.2648	0.4252	0.0559	0.4476
B1–B3	0.0009	2.2254	0.4925	2.0613	0.0772	2.1940
TDF(%)	0.0480	10.5239	7.2029	9.3304	1.7869	10.1632

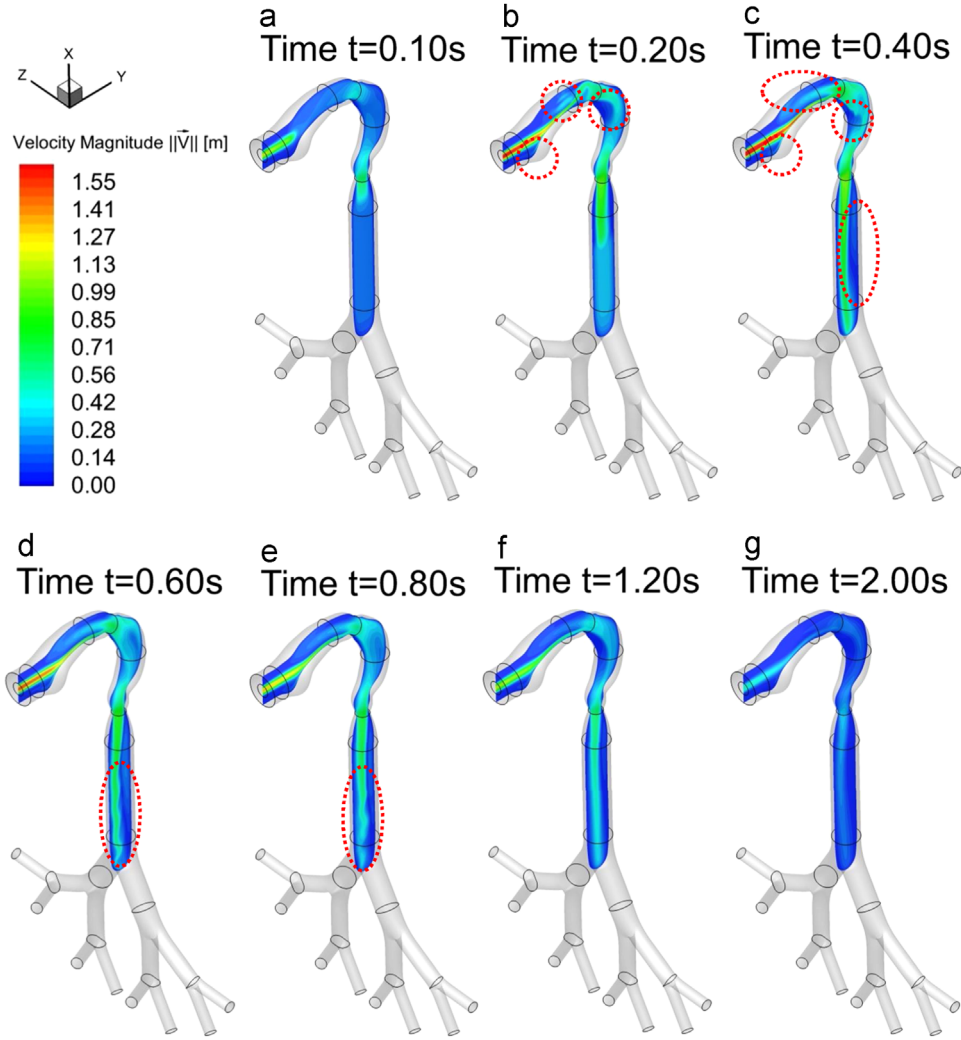


Fig. 9. Airflow field evolution with time for EC-waveform #1: (a) $t=0.1$ s; (b) $t=0.2$ s; (c) $t=0.4$ s; (d) $t=0.6$ s; (e) $t=0.8$ s; (f) $t=1.2$ s; and (g) $t=2.0$ s.

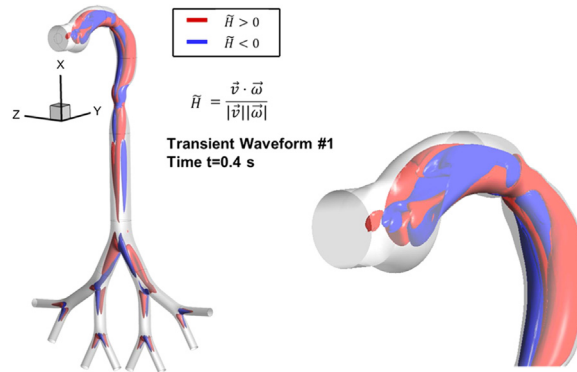


Fig. 10. Visualization of vortices at $t=0.4$ s with waveform #1 when the jet core reaches the first bifurcation – colored by non-dimensionalized helicity H .

side. Another recirculation region is formed at the backside of the trachea (see the red-dash circles in Fig. 9(c)). As the air-drawing intensity decreases after $t=0.6$ s (see Fig. 9(d)–(g)), the jet-core velocity decreases. It is of interest to observe the fluctuating interface between the jet-core and the recirculation region in the trachea (see the red-dash circles in Fig. 9 (d) and (e)). This special flow pattern was only observed for the transient waveform (see Fig. 1(a)) and does not appear under steady inhalation conditions. Similar jet stream and recirculating flow characteristics were reported by Feng and

Kleinstreuer (2011) with a subject-specific human upper lung airway model (mouth to G9). So, the idealized human upper lung airway geometry can be considered to be a representative geometry for capturing major airflow structures.

5.2.1.2. Vortex visualization. Velocity contours alone (see Fig. 9(a)–(g)) are not sufficient to fully depict all airflow structures, especially 3-D vortices and/or secondary flows which cause deposition of inhaled aerosol. Vortices need to be quantitatively identified based on a function that can be evaluated “point-by-point” in order to determine if each flow-field point is inside or outside of the vortex structure. Different vortex identification methods were compared by Jiang, Machiraju, and Thompson (2005) and Roth (2000), where the helicity is defined as

$$H = \vec{v} \cdot \vec{\omega} \quad (33)$$

Degani, Seginer, and Levy (1990) proposed the “helicity method” which utilizes non-dimensionalized helicity, \tilde{H} , for extracting vortex core lines as

$$\tilde{H} = \frac{\vec{v} \cdot \vec{\omega}}{|\vec{v}| |\vec{\omega}|} \quad (34)$$

where \tilde{H} is the cosine of the angle between local velocity \vec{v} and vorticity $\vec{\omega}$ (the curl of \vec{v}). Degani et al. (1990) proposed that the vortex-core line (or axis) is a curve where the vorticity $\vec{\omega}$ tends to align with the velocity \vec{v} , i.e., \tilde{H} . Furthermore,

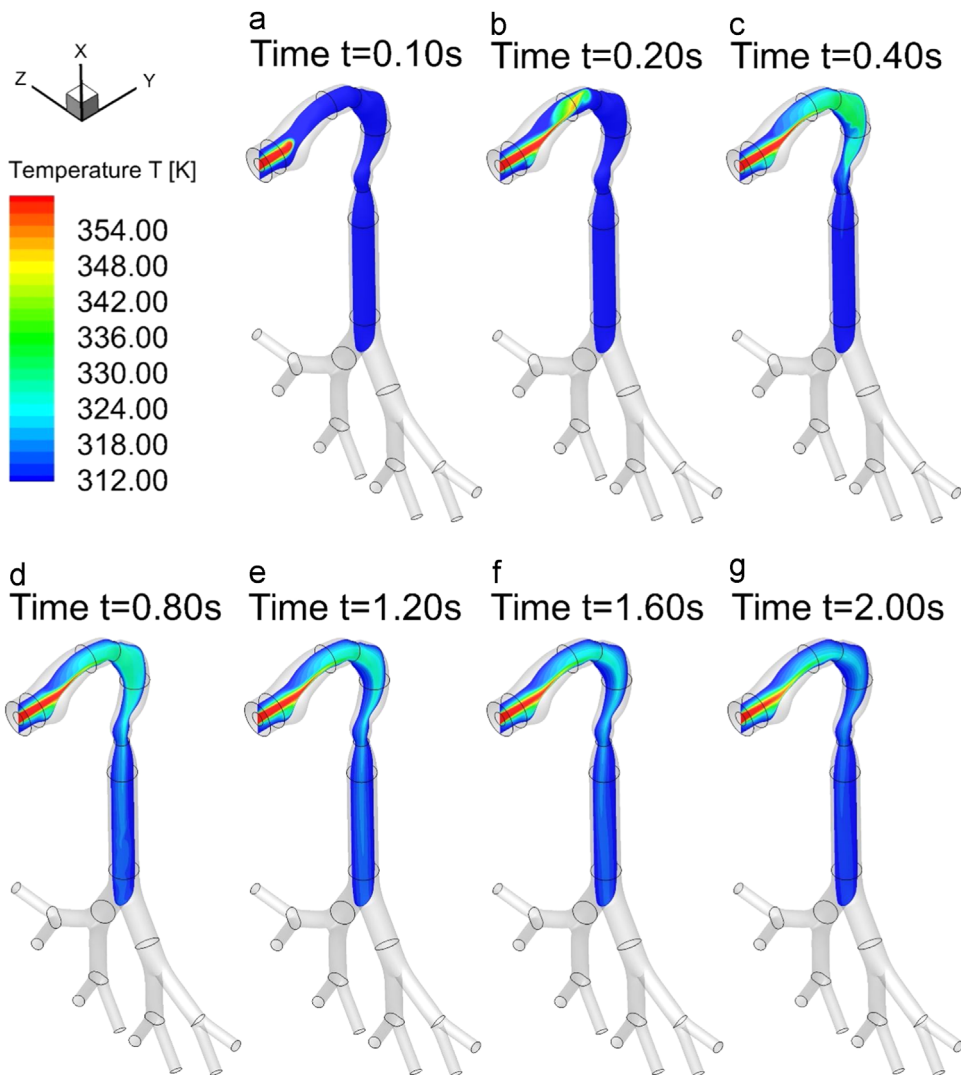


Fig. 11. Temperature field evolution with time for EC-waveform #1: (a) $t=0.1$ s; (b) $t=0.2$ s; (c) $t=0.4$ s; (d) $t=0.8$ s; (e) $t=1.2$ s; (f) $t=1.6$ s; and (g) $t=2.0$ s.

the sign of \tilde{H} indicates the direction of the vortex (clockwise or counterclockwise) with respect to the streamwise velocity vector.

Using the helicity method, the major vortex structures are visualized at $t=0.4$ s when the inlet jet-core has reached the first bifurcation (see Fig. 10). As shown in Fig. 10, several pairs of vortices are generated due to the high-velocity jet in the oral cavity near the mouth inlet. Before entering the contraction between the oral cavity and pharynx, Dean-type vortices swirl towards the upper palate near the wall and towards the lower palate near the sagittal plane ($Z=0$). Entering the pharynx, glottis and trachea, vortex structures remain and intertwine. Double vortices can also be observed near each bifurcation point from G1 to G3. Such local Dean-type vortices were also observed for steady airflow structures in human lung airway bifurcations (Feng, 2013). These vortices are capable of enhancing the local heat and mass transfer in the human respiratory system; thus, influencing local EC-aerosol transport and deposition.

5.2.2. Temperature field

The evolution of the temperature field when using the transient puff waveform #1 is shown in Fig. 11(a)–(g). Upstream to the location where the inlet jet impacts the lower palate, the high-temperature core ($T=360.15$ K) is concentrated without much diffusion. In contrast, jet-stream impaction onto the lower palate leads to more complex secondary flow patterns (see Figs. 9(a)–(g) and 11), which enhances local heat transfer. As a result, during the whole puff cycle the temperature is more evenly distributed in the pharynx (see Fig. 11(a)–(g)). Furthermore, the local temperature distribution during puffing in the human upper lung airway from mouth to G1 varies; hence, it will influence condensation or evaporation and thereby leading to different droplet-size changes as well as local vapor concentrations and compound depositions.

5.2.3. Species transport and deposition patterns in vapor form

Given the initial liquid–vapor partitions shown in Table 1, all three species, i.e. glycerol, PG and nicotine, undergo continuous condensation. Hence, local vapor transport patterns among the three species are similar and so only local nicotine-vapor transport and deposition at different time steps has been tracked, being the most important of the

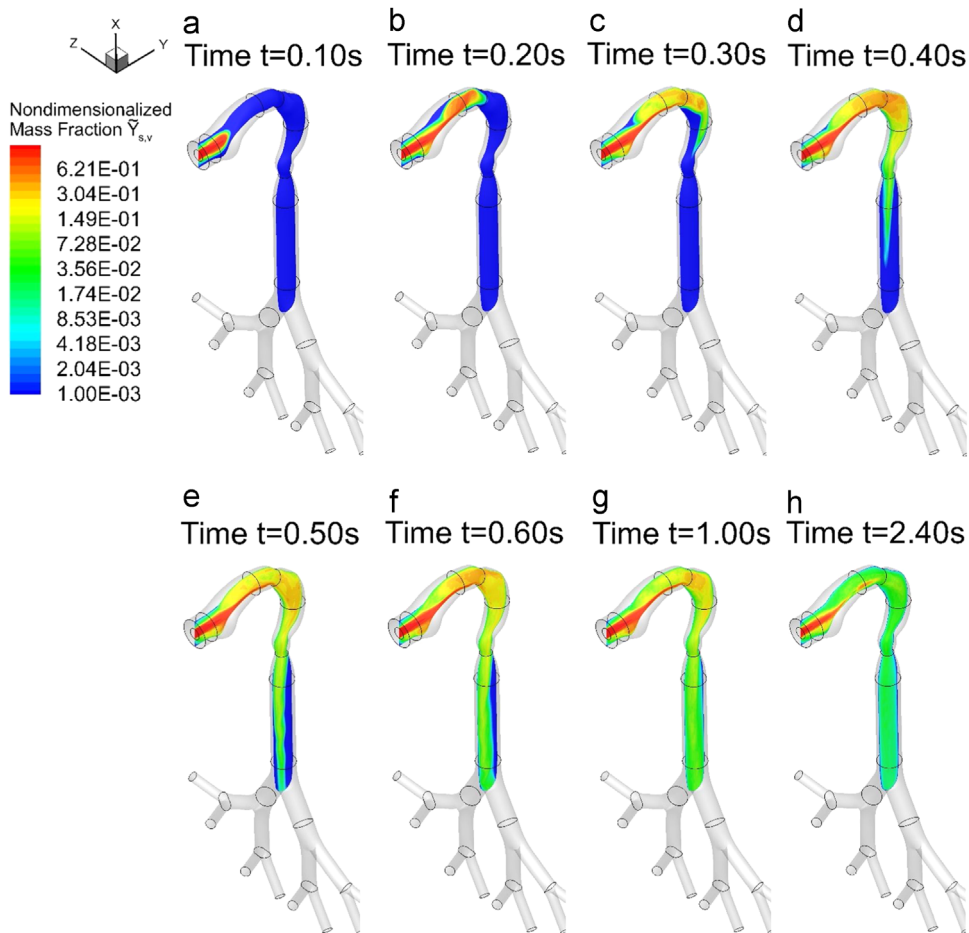


Fig. 12. Contours of non-dimensionalized nicotine vapor mass fraction $Y_{s,v} = Y_{s,v}^{(in)}$ in the sagittal plane ($Z=0$) of the idealized human upper airway geometry at different times: (a) $t=0.1$ s; (b) $t=0.2$ s; (c) $t=0.3$ s; (d) $t=0.4$ s; (e) $t=0.5$ s; (f) $t=0.6$ s; (g) $t=1.0$ s; and (h) $t=2.4$ s.

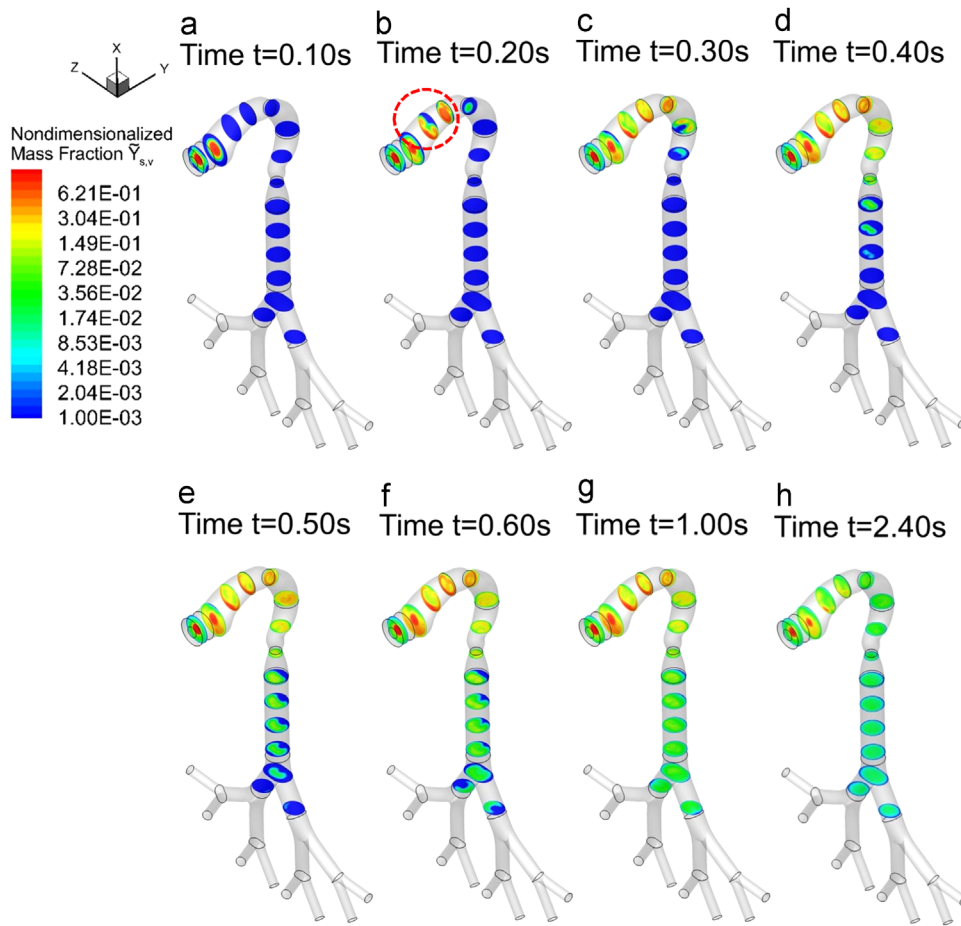


Fig. 13. Contours of non-dimensionalized nicotine vapor mass fraction $\tilde{Y}_{s,v} = Y_{s,v}/Y_{s,v}^{(in)}$ at different cross sections perpendicular to the centerline of the idealized human upper airway geometry at different times: (a) $t=0.1$ s; (b) $t=0.2$ s; (c) $t=0.3$ s; (d) $t=0.4$ s; (e) $t=0.5$ s; (f) $t=0.6$ s; (g) $t=1.0$ s; and (h) $t=2.4$ s.

compounds (see Figs. 12–14). The regional and total deposition data are listed in Table 5 and visualized in Fig. 20. Non-dimensionalized vapor mass fraction $\tilde{Y}_{s,v}$, depicted in Figs. 12 and 13, is calculated as

$$\tilde{Y}_{s,v} = Y_{s,v}/Y_{s,v}^{(in)} \quad (35)$$

where $Y_{s,v}^{(in)}$ is the nicotine-vapor mass fraction at the mouth inlet.

Compared to the airflow field structure at different time steps (see Figs. 9(a)–(g) and 10), nicotine-vapor transport is determined by both convection and diffusion, where the local concentration is also influenced by condensation/evaporation between droplets and vapors. At $t=0.1$ s (see Figs. 12(a) and 13(a)), nicotine-vapor follows the air-inlet jet with some diffusion, similar to the temperature (see Fig. 11(a)). At $t=0.2$ s, just after the inlet jet impacts the lower palate, higher concentrations of nicotine vapor exist closer to the lower palate (see the red dashed circle in Fig. 13(b)) where the double-vortex in the oral cavity enhances mixing of the high concentration nicotine vapor with the low concentration nicotine vapor near the upper palate (see Fig. 13(b)). From $t=0.3$ s to 0.5 s (see Figs. 12(c)–(f) and 13(c)–(f)) reaching the first bifurcation, the distribution of the nicotine-vapor mass fraction at different cross sections follows the local secondary flow structures (see Fig. 10). Specifically, the recirculating flow (see Fig. 9(c)) enhances nicotine-vapor mixing in the pharynx (see Fig. 12(d)). The jet core towards the front of the trachea (see Fig. 9(c) and (d)) also carries high-concentration nicotine vapor in the same direction (see Fig. 12(d) and (e)). Later on, nicotine vapor becomes more and more evenly distributed from mouth to G3 due to the secondary-flow induced mixing and diffusion effects (see Figs. 12(g), (h) and 13(g), (h)).

Figure 14(a)–(g) show the accumulated nicotine-vapor deposition surface density $\rho_A^{(dep)}$ [kg/m^2] at different time levels. As expected, nicotine vapor deposits gradually from the mouth to G3, while the transport and deposition downstream experiences a delay. Enhanced deposition occurs near the EC exit (or mouth inlet), lower palate, anterior part of the oral cavity, the outside bend of the pharynx, and bifurcation points. This is due to the large concentration gradients induced by direct impaction or long residence times of nicotine vapor in recirculation regions with complicated secondary flow structures.

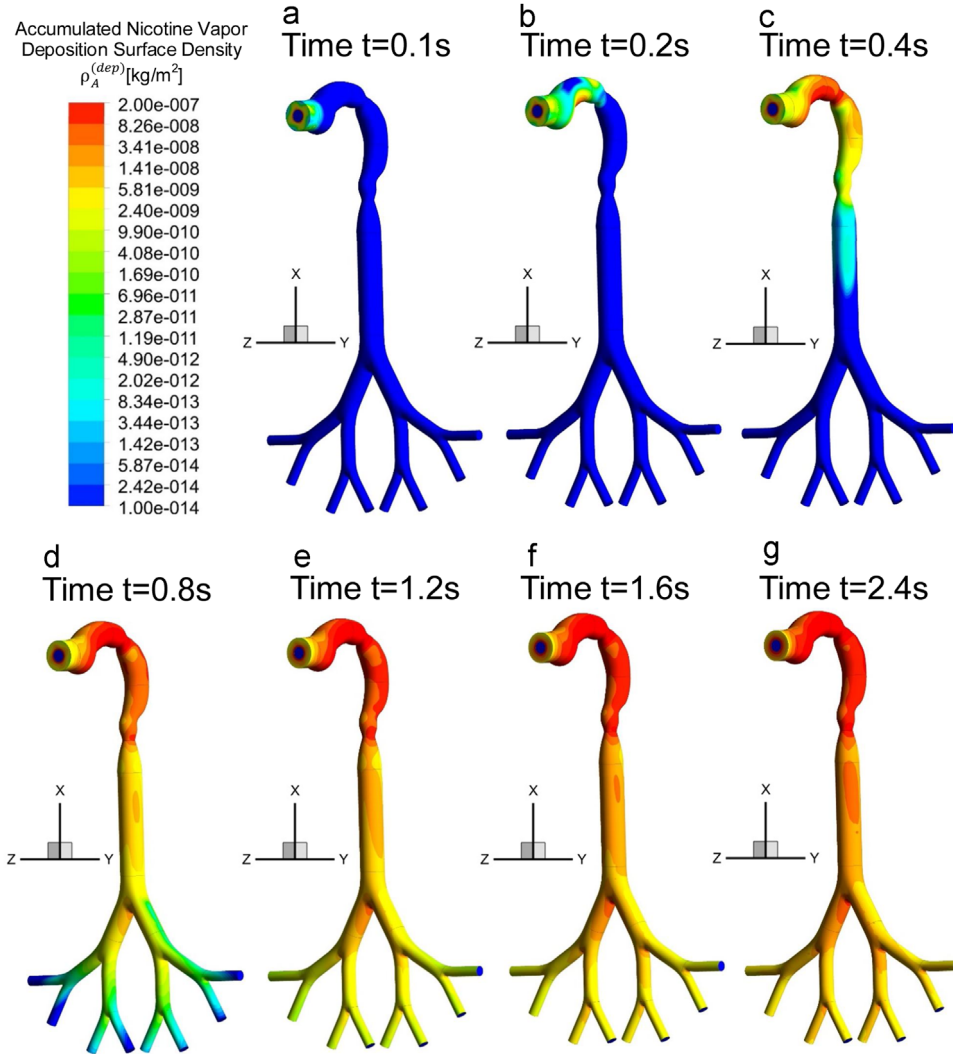


Fig. 14. Contours of surface density [kg/m^2] of nicotine-vapor deposition for EC-waveform #1 at different times: (a) $t=0.1$ s; (b) $t=0.2$ s; (c) $t=0.4$ s; (d) $t=0.8$ s; (e) $t=1.2$ s; (f) $t=1.6$ s; and (g) $t=2.4$ s.

5.2.4. Species transport and deposition patterns in liquid form with droplet size change dynamics

The transport and deposition of EC-smoke constituents in liquid form is associated with the nanodroplet dynamics, i.e., transport, size change and deposition, as shown in Figs. 15(a)–(f) and 16(a), (b). Droplets are colored by its instantaneous diameter which is influenced by the condensation/evaporation effects interacting with the ambient vapor phases.

For the EC-droplet transport and size dynamics shown, the suspended EC droplets with $d_{d,ini}=400$ nm keep absorbing vapors from the ambient and hence growing in size. Some droplets are able to follow closely the air-jet, as can be observed when considering the share of droplets forming the stream's frontier. Meanwhile, other droplets escape from the mainstream due to the combined effects of Brownian motion and local secondary flows, thereby aggregating near the lung-airway surfaces where the air velocity is low. Thus, before the glottis at the same cross-sectional plane perpendicular to the airway centerline, droplets closer to the center have smaller diameters because of the relatively low residence time due to the locally higher velocity. After the contraction in the glottis, the same effect is not obvious. It is worth mentioning that at $t=0.5$ s, the frontier of the droplets reaches G1, and at $t=0.8$ s it reaches G3. Additionally, at $t=0.6$ s and 0.8 s (see Fig. 15 (c) and (d)), due to the lower pressure near the inner wall downstream of the first bifurcating point, droplets are driven towards the inner wall. However, as time evolves, some droplets also escape and get suspended in the region closer to the outer wall (Fig. 15(e) and (f)). The maximum growth ratio at the end of the single puff cycle ($t=2.4$ s) is about 2.18. Figure 16 (a) and (b) show the local deposition patterns of droplets at the end of the single puff and after one-second holding, colored by their final diameter.

Multiple deposition mechanisms determine different deposition patterns from mouth to G3. Favorable spots for droplet deposition include the lower palate, back of the pharynx, glottis and regions near each bifurcation point. Droplets with low

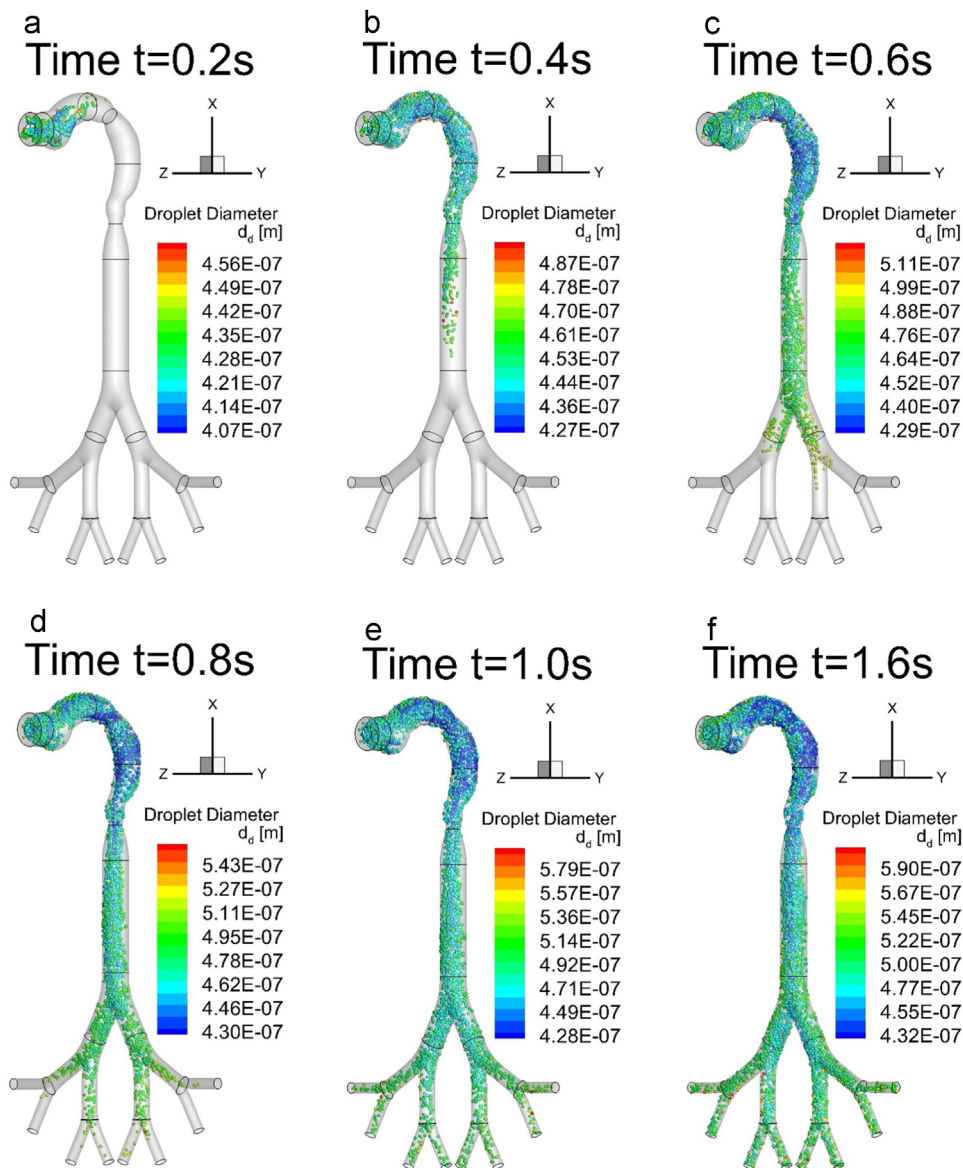


Fig. 15. EC-droplet transport and size change dynamics for waveform #1 at different times: (a) $t=0.2$ s; (b) $t=0.4$ s; (c) $t=0.6$ s; (d) $t=0.8$ s; (e) $t=1.0$ s; and (f) $t=1.6$ s.

residence times experience relatively small growth rates and deposit typically via direct impaction, as in the oral cavity. However, there are other droplets deposited in the oral cavity with somewhat larger size. Such depositions occur because of Brownian motion and secondary flow effects, i.e., they had longer residence times and thereby more time to absorb ambient vapors to grow larger.

5.3. Parametric sensitivity analyses: impact of puffing/inhalation patterns on EC aerosol deposition

The impacts of different steady and transient inhalation patterns on aerosol deposition were simulated. Table 3 and Fig. 1 (a), (b) show several puff volumes and durations studied here.

5.3.1. Inhalation flow rate

The impact of inhalation flow rate on EC-aerosol transport and deposition was investigated by first fixing the steady puffing duration at different flow rates (i.e., $Q_{in}=12, 20$, and 27.5 ml/s at $t=2$ s) and then fixing the total puff volume (i.e., 27.5 ml/s at $t=2$ s and 18.33 ml/s at $t=3$ s). Histograms of regional and total deposition fractions (RDFs and TDFs) of glycerol, PG and nicotine in both vapor and liquid forms for the four cases are given in Figs. 17–19.

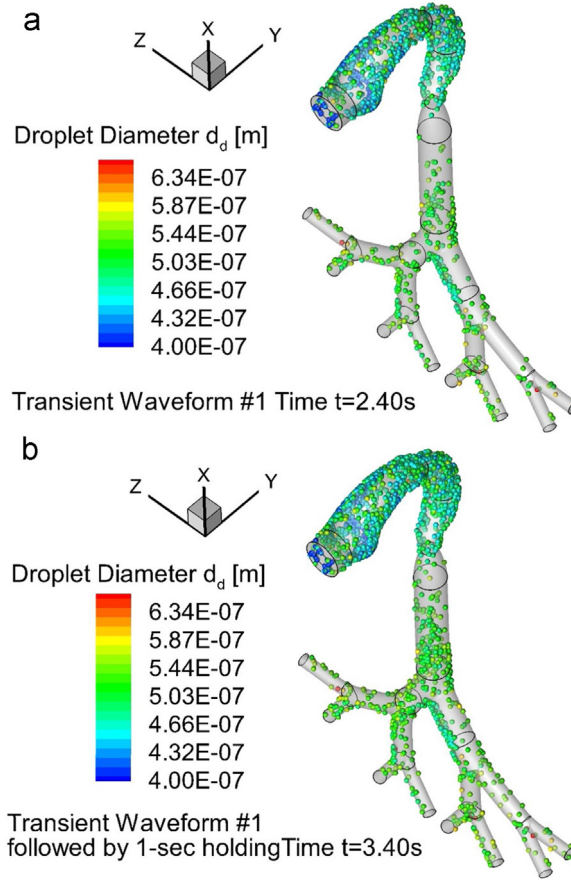


Fig. 16. EC-droplet deposition colored by final diameter: (a) for waveform #1 at $t=2.4$ s and (b) for waveform #1 followed by one-second holding at $t=3.4$ s.

5.3.1.1. *Fixed puff duration ($t=2$ s) at different flow rates ($Q_{in}=12, 20$, and 27.5 ml/s).* Overall, absorption of all three species in vapor form (see Figs. 17(a), 18(a) and 19(a)), being less than in liquid form, has in all regions a consistent upward trend with increasing flow rate as recorded after $t=2$ s. In contrast, there are no consistent regional correlations between absorption values for PG, glycerol and nicotine in liquid form and the magnitudes of inhalation flow rates (see Figs. 17(b), 18(b), and 19(b)), resulting in almost uniform total deposition efficiencies for all three flow rates after $t=2$ s.

Specifically, for species deposition in *vapor form* shown in Figs. 17(a), 18(a), and 19(a) the following observations can be made:

- In the oral cavity, oropharynx, trachea and B1–B3, vapor absorption fractions $DF_{s,v}$ increase after 2 s with higher inlet flow rates. This is mainly due to direct impaction and secondary flows, as regionally a lower inhalation flow rate implies a longer droplet-residence time, providing extra time for the species in vapor form to condensate. This also explains, at least for the oral-cavity, the opposite trend of nicotine deposition in liquid form (see Figs. 17(b), 18(b), and 19(b)). Lower flow rates also delay the convective transfer of vapor into lower lung airways, which is another mechanism to influence the local vapor concentration and absorption rate.
- For a fixed inhalation duration of, say, $t=2$ s, stronger drawing (e.g., 27.5 ml/s) will result in a more evenly distributed nicotine vapor absorption, $DF_{s,v}$, from the oral cavity to B3.
- Simultaneously, stronger drawing (e.g., 27.5 ml/s) will induce higher TDFs for all vapor species.

Concerning species deposition in *liquid form*, as shown in Figs. 17(b), 18(b) and 19(b), one can conclude the following:

- In the oral cavity, the species regional deposition fractions (RDFs) in liquid form, $DF_{s,l}$, after $t=2$ s decrease with higher inlet flow rates as the result of several mechanisms, i.e.,
 - at lower inlet flow rates, the longer residence times for droplets in the oral cavity lead to increased chances for deposition due to Brownian motion, secondary flows, and sedimentation;
 - a longer transport time before reaching the lower palate also increases the hygroscopic growth of droplets, thereby strengthening direct impaction; although, the inlet flow rates are still relatively low.
- In the oropharynx, no monotonic trend in RDFs can be observed with increased inlet flow rates, as different deposition mechanisms are in effect.

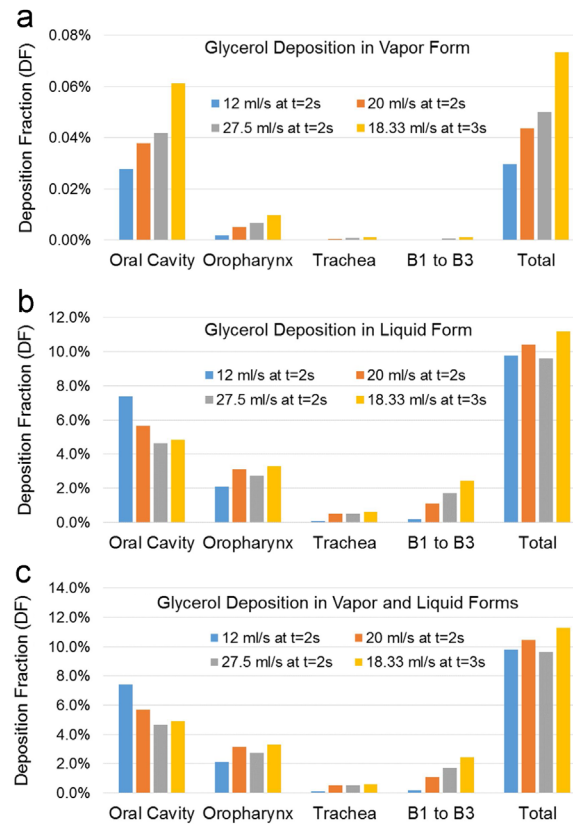


Fig. 17. Regional and total deposition fractions of glycerol considering four different steady puffing scenarios: (a) deposition fractions in vapor form; (b) deposition fractions in liquid form; and (c) deposition fractions in both vapor and liquid forms.

- In the trachea and B1–B3, the RDFs after $t = 2$ s increases with higher inlet flow rates, due to stronger Brownian motion with less hygroscopic growth, stronger direct impaction, and secondary flow effects.
- Again, if the inhalation duration is fixed, i.e., $t = 2$ s, stronger drawing (e.g., 27.5 ml/s) will induce a more evenly-distributed species absorption from the oral cavity to B3.
- The selected range of inhalation flow rates (from 12 ml/s to 27.5 ml/s) has no significant impact on the species' total deposition fractions (TDFs), and no monotonic trend can be observed due to the different RDF occurrences. For the total species depositions depicted in Figs. 17(c), 18(c) and 19(c), the following can be noted:
- Due to the higher DF-differences of all species in liquid form than in vapor form, the impact of flow rate on DF_s has the same trend as the RDF-trends in liquid form, i.e., $DF_{s,v+1}(t)$.
- If the inhalation duration is fixed, i.e., $t = 2$ s, stronger drawing (e.g., 27.5 ml/s) will induce more evenly-distributed species absorption from the oral cavity to B3.
- The inhalation flow rate (from 12 ml/s to 27.5 ml/s) has no significant impact on the total deposition fractions of all species in the upper lung airways from mouth to G3.

5.3.1.2. Fixed total puff volume (55 ml) with different puff flow rates ($Q_{in} = 27.5$ ml/s and 18.33 ml/s). To further investigate the influence of inhalation waveform on species transport and deposition, two different puffing conditions with the same total puff volume (i.e., 55 ml) were simulated and compared (Figs. 17–19). With the same puff volume, lower air-drawing intensity, e.g., 18.33 ml/s, induces higher RDFs in all regions, i.e., from the mouth to G3 for the following reasons:

- Longer vapor residence time induces higher vapor absorption/deposition.
- Longer droplet residence time induces a higher probability of deposition.

It can also be observed that in the four cases investigated, all three species are fast absorbed in the oral cavity and oropharynx because of the longer vapor and droplet residence times as well as larger airway-surface areas. Furthermore, except for the absorption coefficient, the initial liquid–vapor partitions and volatilities also influence the deposition of vapors. Specifically, glycerol deposition in vapor form is negligible compared to its deposition in liquid form because of the initial liquid–vapor partition containing only 0.1293% glycerol vapor due to the low volatility. In contrast, PG deposition in

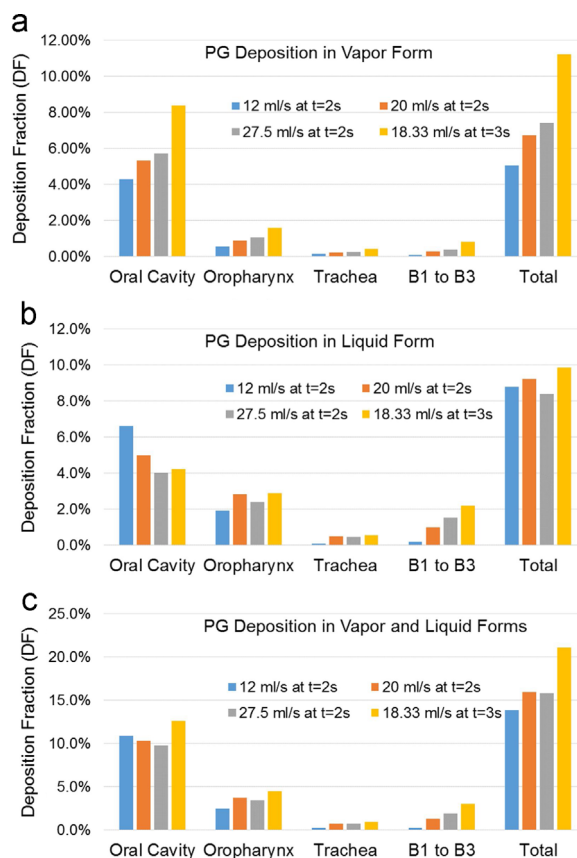


Fig. 18. Regional and total deposition fractions of PG considering four different steady puffing scenarios: (a) deposition fractions in vapor form; (b) deposition fractions in liquid form; and (c) deposition fractions in both vapor and liquid forms.

vapor form is comparable to the deposition in liquid form, which is due to the initial partition based on its relatively high volatility.

5.3.2. Influence of holding duration on deposition for transient waveform #1

Most publications focusing on smoke-aerosol deposition in human lung models did not include the holding phase after puffing. To further investigate the influence of holding duration on deposition, results from two scenarios were compared, i.e., waveform #1 (see Fig. 1(a)) after $t = 2.4$ s and with one-second holding after $t = 3.4$ s. Nicotine deposition data are shown in Fig. 20(a)–(c), representing also the trends of the other two species (i.e., glycerol and PG). It is obvious that the extra one-second holding increases the regional and total depositions of nicotine in both vapor and liquid forms. Indeed, a longer holding phase after puffing will result in higher depositions due to vapor diffusion and some droplets already near the airway walls. Considering the droplet deposition pattern shown in Fig. 16(a) and (b), with the one-second holding the average droplet growth ratio is higher and so is the number of droplets deposited.

5.3.3. Transient waveform #1 (CC-users) vs. transient waveform #2 (EC-users)

Waveforms #1 vs. waveform #2 represents contrasting EC-puffing behavior by a conventional cigarette user and an EC-user for the same total puff volume (i.e., 63.9 ml), but different puff durations and peak flow rates (Fig. 1(a) and (b)). The comparisons of nicotine deposition in vapor and liquid forms are also shown in Fig. 20(a)–(c). Although Fig. 20(c) still indicates that if the total puff volume is fixed, waveform #2 with a lower puff intensity will induce higher total deposition, i.e., the RDFs in vapor or liquid forms are not monotonically increasing or decreasing. The results differ from the steady-state puffing outcome (see Section 5.3.1). The complexity is introduced by the transient airflow fields, as they have more variations in local secondary flows, resulting in a more complex deposition scenario of droplets as well as local vapor absorption.

In summary, EC-users who are accustomed to EC-products have a puffing behavior (i.e., waveform #2) which leads to elevated nicotine uptakes in the upper lung airways when compared to CC-users with waveform #1.

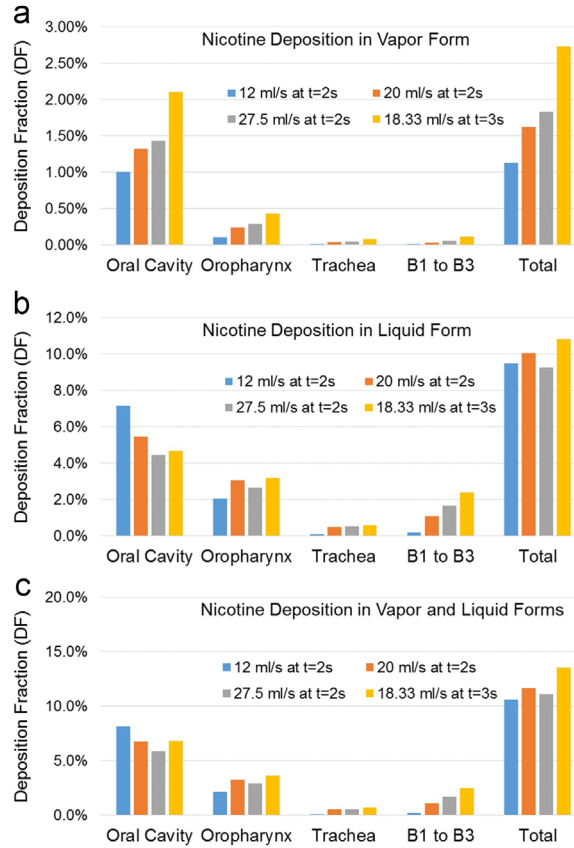


Fig. 19. Regional and total deposition fractions of nicotine considering four different steady puffing scenarios: (a) deposition fractions in vapor form; (b) deposition fractions in liquid form; and (c) deposition fractions in both vapor and liquid forms.

5.4. Parametric sensitivity analyses: impact of inhalation patterns on EC liquid–vapor interaction

To provide more physical insight on liquid–vapor interactions, comparisons of vapor–liquid mass change percentages for the three compounds as well as droplet–growth ratios were evaluated for different puffing patterns. The vapor–liquid mass change percentage of the s th species $\beta_{v-l,s}(t)$ is

$$\beta_{v-l,s}(t) = \frac{m_{s,v}^{(in)} - (m_{s,v}^{(dep)} + m_{s,v}^{(sus)} + m_{s,v}^{(out)})}{m_{s,v}^{(in)}} \times 100\% \quad (36)$$

where $m_{s,v}^{(in)}$, $m_{s,v}^{(sus)}$, $m_{s,v}^{(dep)}$ and $m_{s,v}^{(out)}$ are the accumulated inflow mass, suspended mass, deposition mass, and outflow mass of vapor species. A negative value of $\beta_{v-l,s}(t)$ indicates net evaporation, while a positive value implies net condensation. The droplet–growth ratio (GR) at time t is

$$GR(t) = \frac{d_d(t)}{d_{d,ini}} \quad (37)$$

For all three species, i.e., glycerol, PG and nicotine, under the steady two-second-puff condition, Fig. 21(a) indicates that a lower inlet flow rate will cause a higher vapor–liquid mass transfer percentage. This is probably due to the longer droplet residence time allowing for extended droplet–vapor interactions. Figure 21(a) also shows a comparison among the three transient puffing cases. It can be observed that the additional one-second holding yields a slightly higher mass transfer percentage, which is also due to the longer droplet residence time. With the fixed total puff volume (i.e., 63.9 ml), lower inhalation intensity case (see waveform #2) provides higher mass change percentages for all three species.

Figure 21(b) illustrates the size-change dynamics of suspended droplets ($d_{d,ini}=400$ nm) under different puffing conditions. Due to the continuous condensation effect, the average droplet GR gradually increases with time for all puffing scenarios. For steady puffing, combined with the observations given in Fig. 21(a), a lower inlet flow rate induces a higher mass transfer percentage, i.e., a stronger condensation effect, thereby leading to a higher average droplet GR than the stronger inhalation case. The increasing GR-rate (i.e., the slope of the curve) gradually decreases, indicating the liquid–vapor interactions gradually reach a quasi-equilibrium state. However, for the transient puffing case shown in Fig. 21(b), the

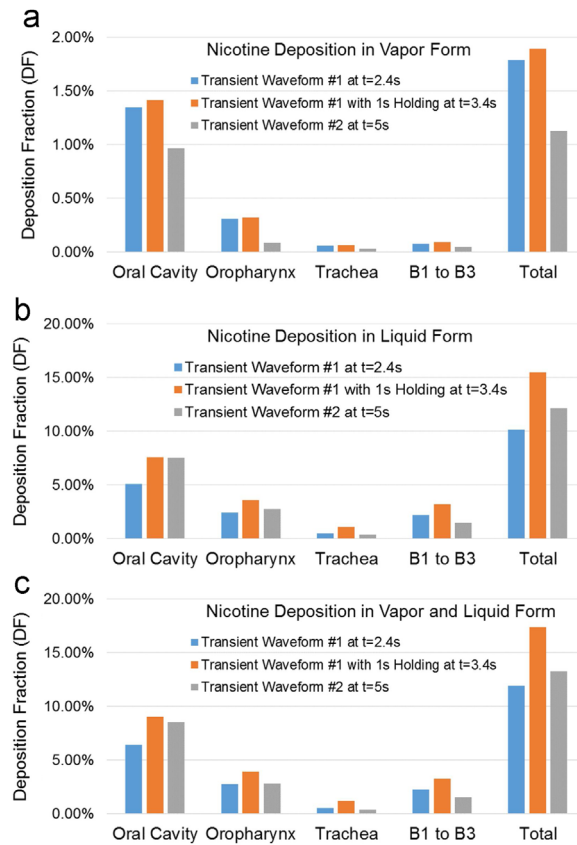


Fig. 20. Regional and total deposition fractions of nicotine for different transient EC-smoke inhalation conditions (i.e., waveform #1, waveform #1 with one-second holding, and waveform #2): (a) deposition fractions in vapor form; (b) deposition fractions in liquid form; and (c) deposition fractions in both vapor and liquid forms.

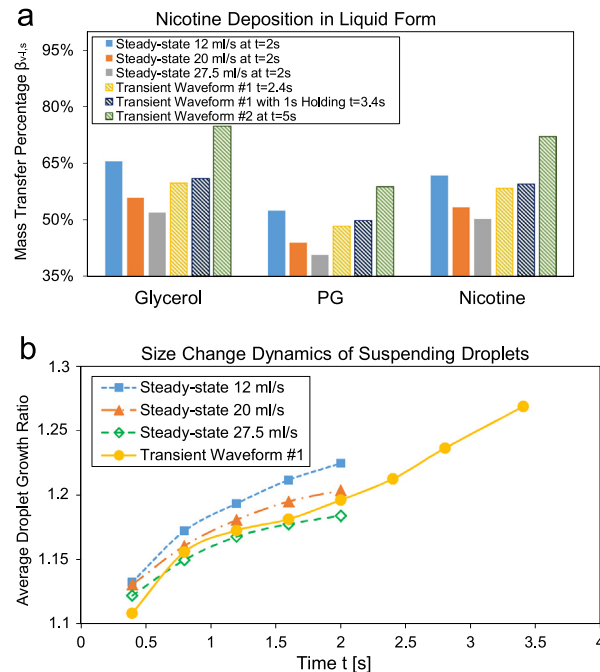


Fig. 21. Comparisons of key aspects of droplet-vapor dynamics for different puffing scenarios: (a) percentage-changes in liquid-vapor mass transfer and (b) averaged droplet-size growth ratio.

increasing GR-rate is not monotonic with time. This is because of the variation in inhalation flow rate during the transient puffing cycle. Specifically, after 2.4 s holding starts and no air and EC aerosols are being further inhaled until 3.4 s. The average droplet-GR increases at a faster rate because of the increasing RH in the lung airways and the near-static airflow field exhibiting weak convection.

6. Conclusions

A novel CF-PD model, based on the MCM-DD approach, has been developed which can simultaneously simulate transport and deposition of interactive, multicomponent droplet–vapor mixtures in human lung–airways. At present, the focus is on two-phase EC–nicotine absorption in an idealized human upper airway model, subject to different puffing/inhalation scenarios. Because of the high particle concentration, a scale-factor correlation was introduced, as part of the IRD method, to achieve realistic deposition data. It should be noted that the MCM-DD model can be extended to other components to evaluate potential health risks of additional constituents present in EC–smoke. Other applications of the model include analysis of propulsion fuels and drug–aerosols.

Selected EC–aerosol compositions are listed in Table 1 for realistic computer inputs. With the comparisons of deposition and interaction results under different EC–smoking modes, the major conclusions are as follows:

- (a) Complex secondary flows and Dean-type vortices exist throughout the idealized mouth-to-G3 human upper lung airway model which significantly influence droplet transport and distribution. It is of interest to note that the major flow patterns captured in the idealized human upper lung airways appear also in subject-specific models.
- (b) Droplet–vapor interaction mechanisms must be considered, as they have a strong impact on deposition predictions of inhaled EC aerosols.
- (c) EC–aerosol deposition mechanisms includes direct impaction, Brownian motion, secondary flows, recirculating flows with enhanced residence times, and gravitational sedimentation.
- (d) At a fixed inhalation duration (e.g., $t = 2$ s) for steady puffing, stronger air-drawing will induce more evenly distributed depositions in the mouth-to-G3 region, less vapor–liquid mass transfer percentages, and lower average droplet–growth ratios.
- (e) For a fixed puff volume at steady inhalation, stronger drawing will lead to lower regional and total depositions in both vapor and liquid forms for all species. However, for the two transient waveforms (see Fig. 1(a) and (b)), stronger drawing will not induce monotonic changes in all regional depositions, but it will still induce lower total depositions.
- (f) Longer droplet–vapor holding after puffing results in to higher deposition fractions, higher vapor–liquid mass transfer percentages, and higher average droplet–growth ratios. Hence, for accurate uptake predictions, it is necessary to simulate not only the puffing/inhalation process but also the holding action.

7. Future work

In light of the necessary simplifications made and the current lack of experimental deposition data for E–cigarettes, improvements are suggested as follows:

- (a) Development of a generalized SF-function with extended dependence on droplet diameter, droplet composition, liquid–vapor partition, RH, and lung–airway geometry.
- (b) Further investigation of inter-subject variability using different models of human respiratory systems.
- (c) Additional parametric sensitivity analyses with excessive compound concentrations, presence of variable mucus layers, different aerosol–inhalation waveforms, EC–aerosols vs. CC–smoke particles, second-hand smoke inhalation, etc.
- (d) Adjustment of model–parameter/coefficient values and hence impact evaluation as new experimental data sets appear. Of special interest are:
 - Inhalation/puffing waveforms for ECs
 - Reliable saturation pressure measurements for PG, glycerol, nicotine, formaldehyde, flavor chemicals, etc.
 - Liquid–vapor partitions for PG, glycerol, nicotine, and other species of interest
 - Activity coefficients of all species in EC multicomponent droplets
 - Compound parameter values, e.g., absorption coefficients between air and mucus layer.
- (e) Consideration of cloud–formation/motion effects, charge effects, and coagulation

Acknowledgments

The authors are grateful for the financial support of Y. F. by a grant from NSF (CBET-1232988), Environmental Health and Safety of Nanotechnology, and by Altria Client Service LLC (ALCS). Insightful discussions with Dr. Pithawalla from ALCS (Richmond, VA) are appreciated as well.

References

- Alderman, S. L., Song, C., Moldoveanu, S. C., & Cole, S. K. (2014). Particle size distribution of E-cigarette aerosols and the relationship to Cambridge filter pad collection efficiency. *Beiträge zur Tabakforschung/Contributions to Tobacco Research*, 26(4), 183–190.
- Behar, R. Z., Hua, M., & Talbot, P. (2015). Puffing topography and nicotine intake of electronic cigarette users. *PLoS One*, 10(2), e0117222.
- Canada. (2014). *Canada Government Tobacco Act: Tobacco Reporting Regulations, SOR/2000-273, Part 3: Emissions from designated tobacco products*. Health Canada.
- Cheng, Y. S., Zhou, Y., & Chen, B. T. (1999). Particle deposition in a cast of human oral airways. *Aerosol Science and Technology*, 31(4), 286–300.
- Degani, D., Seginer, A., & Levy, Y. (1990). Graphical visualization of vortical flows by means of helicity. *AIAA Journal*, 28(8), 1347–1352.
- Eatough, D. J., Benner, C. L., Bayona, J. M., Richards, G., Lamb, J. D., Lee, M. L., Lewis, E., & Hansen, L. D. (1989). Chemical composition of environmental tobacco smoke. 1. Gas-phase acids and bases. *Environmental Science Technology*, 23(6), 679–687.
- Evans, S. E., & Hoffman, A. C. (2014). Electronic cigarettes: Abuse liability, topography and subjective effects. *Tobacco Control*, 23(Suppl. 2), ii23–ii29.
- Fahy, J. V., & Dickey, B. F. (2010). Airway mucus function and dysfunction. *New England Journal of Medicine*, 363(23), 2233–2247.
- Farsalinos, K. E., Spyrou, A., Tsimopoulou, K., Stefanopoulos, C., Romagna, G., & Voudris, V. (2014). Nicotine absorption from electronic cigarette use: Comparison between first and new-generation devices. *Scientific Reports*, 4.
- Feng, Y. (2013). *Non-spherical particle dynamics analysis with applications to inhaled aerosol transport and deposition in human upper airway models* (Ph.D. dissertation). Raleigh, NC: NC State University.
- Feng, Y., & Kleinstreuer, C. (2011). Computational analysis of droplet evaporation and deposition in a realistic respiratory tract subject to puff-like inhalation waveforms. In *Proceedings of the 2nd International Conference on Computational & Mathematical Biomedical Engineering (CMBE11)*. Washington, DC, USA.
- Feng, Y., Kleinstreuer, C., & Rostami, A. (2015). Evaporation and condensation of multicomponent electronic cigarette droplets and conventional cigarette smoke particles in an idealized G3–G6 triple bifurcating unit. *Journal of Aerosol Science*, 80, 58–74.
- Gowadia, N., & Dunn-Rankin, D. (2010). A transport model for nicotine in the tracheobronchial and pulmonary region of the lung. *Inhalation Toxicology*, 22(1), 42–48.
- Gupta, D., & Peters, M. H. (1985). A Brownian dynamics simulation of aerosol deposition onto spherical collectors. *Journal of Colloid and Interface Science*, 104(2), 375–389.
- Hayduk, W., & Laudie, H. (1974). Prediction of diffusion coefficients for nonelectrolytes in dilute aqueous solutions. *AIChE Journal*, 20(3), 611–615.
- Hinds, W. C. (1999). *Aerosol technology: Properties, behavior, and measurement of airborne particles* ((2nd ed.). New York, USA: John Wiley & Sons.
- ICRP. (1994). Human respiratory tract model for radiological protection. ICRP publication 66. *Annals of the ICRP*, 24, 1–3.
- Jiang, M., Machiraju, R., & Thompson, D. (2005). Detection and visualization of vortices. In *The visualization handbook* (295 pp.). Academic Press.
- Johnson, T. J., Olfert, J. S., Yurteri, C. U., Cabot, R., & McAughey, J. (2015). Hygroscopic effects on the mobility and mass of cigarette smoke particles. *Journal of Aerosol Science*, 86, 69–78.
- Keyhani, K., Scherer, P. W., & Mozell, M. M. (1997). A numerical model of nasal odorant transport for the analysis of human olfaction. *Journal of Theoretical Biology*, 186(3), 279–301.
- Lee, Y. H., Gawron, M., & Goniewicz, M. L. (2015). Changes in puffing behavior among smokers who switched from tobacco to electronic cigarettes. *Addictive Behaviors*, 48, 1–4.
- Li, W., & Hopke, P. K. (1993). Initial size distributions and hygroscopicity of indoor combustion aerosol particles. *Aerosol Science and Technology*, 19(3), 305–316.
- Lucht, D. L. (1978). The mucous layer of the trachea and major bronchi in the rat. *Scandinavian Electr Micro*, 2, 1089–1098.
- Manigrasso, M., Buonanno, G., Stabile, L., Morawska, L., & Avino, P. (2015a). Particle doses in the pulmonary lobes of electronic and conventional cigarette users. *Environmental Pollution*, 202, 24–31.
- Manigrasso, M., Buonanno, G., Fuoco, F. C., Stabile, L., & Avino, P. (2015b). Aerosol deposition doses in the human respiratory tree of electronic cigarette smokers. *Environmental Pollution*, 196, 257–267.
- Pankow, J. F. (2001). A consideration of the role of gas/particle partitioning in the deposition of nicotine and other tobacco smoke compounds in the respiratory tract. *Chemical Research in Toxicology*, 14(11), 1465–1481.
- Roth, M. (2000). *Automatic extraction of vortex core lines and other line type features for scientific visualization*. Hartung-Gorre.
- Schroeter, J. D., Asgharian, B., Price, O. T., Kimbell, J. S., Kromidas, L., & Singal, M. (2016). Simulation of the phase change and deposition of inhaled semi-volatile liquid droplets in the nasal passages of rats and humans. *Journal of Aerosol Science*, 95, 15–29.
- Shi, H., Kleinstreuer, C., Zhang, Z., & Kim, C. S. (2004). Nanoparticle transport and deposition in bifurcating tubes with different inlet conditions. *Physics of Fluids*, 16(7), 2199–2213.
- Talih, S., Balhas, Z., Eissenberg, T., Salman, R., Karaoghlanian, N., El Hellani, A., Baalbaki, R., Saliba, N., & Shihadeh, A. (2014). Effects of user puff topography, device voltage, and liquid nicotine concentration on electronic cigarette nicotine yield: Measurements and model predictions. *Nicotine & Tobacco Research*, 17(2), 150–157.
- Tian, G., Hindle, M., Lee, S., & Longest, P. W. (2015). Validating CFD predictions of pharmaceutical aerosol deposition with in vivo data. *Pharmaceutical Research*, 1–18.
- Tu, H. H., & Ray, A. K. (2005). Measurement of activity coefficients from unsteady state evaporation and growth of microdroplets. *Chemical Engineering Communications*, 192, 474–498.
- Turns, S. R. (1996). *An introduction to combustion*, Vol. 287. New York, NY, USA: McGraw-Hill.
- Vansickel, Andrea, Edmiston, Jeffery, Liang, Qiwei, Duhon, Cheryl, Liu, Jianmin, Sarkar, Mohamadi (2014). Characterization of electronic cigarette prototype puff topography in adult exclusive cigarette smokers and adult exclusive electronic cigarette users. In *Proceedings of the 20th annual meeting of the Society for Research on Nicotine and Tobacco (SRNT)*. Seattle, WA, February 5–8, 2014.
- Zhang, Z., Kleinstreuer, C., Kim, C. S., & Cheng, Y. S. (2004). Vaporizing microdroplet inhalation, transport, and deposition in a human upper airway model. *Aerosol Science and Technology*, 38(1), 36–49.
- Zhang, Z., Kleinstreuer, C., Donohue, J. F., & Kim, C. S. (2005). Comparison of micro- and nano-size particle depositions in a human upper airway model. *Journal of Aerosol Science*, 36(2), 211–233.
- Zhang, Z., Kleinstreuer, C., & Kim, C. S. (2006). Transport and uptake of MTBE and ethanol vapors in a human upper airway model. *Inhalation Toxicology*, 18(3), 169–184.
- Zhang, Z., & Kleinstreuer, C. (2011). Computational analysis of airflow and nanoparticle deposition in a combined nasal–oral–tracheobronchial airway model. *Journal of Aerosol Science*, 42(3), 174–194.
- Zhang, Z., Kleinstreuer, C., & Hyun, S. (2012a). Size-change and deposition of conventional and composite cigarette smoke particles during inhalation in a subject-specific airway model. *Journal of Aerosol Science*, 46, 34–52.
- Zhang, Z., Kleinstreuer, C., & Feng, Y. (2012b). Vapor deposition during cigarette smoke inhalation in a subject-specific human airway model. *Journal of Aerosol Science*, 53, 40–60.